Forced Plumes in Uniformly Stratified Environment

by

Tamar Stacy-Ann Richards-Thomas

A thesis submitted in partial fulfillment of the requirements for the degree of

Master of Science

in

Department of Earth and Atmospheric Sciences

University of Alberta

Abstract

This research investigates radially spreading intrusion created from a forced plume, when fluid continuously injected vertically from a nozzle entrains uniformly stratified ambient as it falls back upon itself. The flow evolution is determined as it depends upon the ambient buoyancy frequency, N, the source momentum and buoyancy fluxes, M_0 and F_0, respectively. A turbulent forced plume falls to maximum depth, Z_m, rises back upon itself as a fountain to its neutral buoyancy depth, Z_s, then spreads radially outwards. Through theory and experiments we determine that $Z_\mathrm{s} = f(\sigma)H_p$, in which $H_p = M_0^{3/4}F_0^{-1/2}$, $\sigma = (M_0N/F_0)^2$, and $f(\sigma) \propto \sigma^{-3/8}$ for $\sigma \lesssim 50$ and $f(\sigma) \propto \sigma^{-1/4}$ for $\sigma \gtrsim 50$ respectively. In the inertia-buoyancy regime the intrusion front advances in time as $R_\mathrm{f} \propto t^{3/4}$, consistent with models assuming a constant buoyancy flux into the intrusion where the intrusion first forms at radius, R_1, with thickness, h_1, constant in time. The intrusion thickness, $h(r,t)$, adopted a self-similar shape of the form $h/h_1 \simeq [(R_\mathrm{f} - r)/(R_\mathrm{f} - R_1)]^p$, with $p \simeq 0.55 \pm 0.03$. From dense descending plumes in uniformly stratified ambient, we conveniently applied our results to supervolcanoes penetrating and spreading in the stratosphere.

In memory of my mother, Dawn Ann-Marie Richards.

Also dedicated to my father, Horace Richards and my husband, Recy R. Thomas.

Acknowledgement

Contents

List of Figures

List of Tables

List of Symbols

Chapter 1

Introduction and Motivation

The continuous injection of buoyant fluid from an effective point or line source into an unbounded environment creates an unconfined flow that is called a "plume". The motion of plumes is created from the density difference between the source and its environment that generates a continuous supply of buoyancy in the direction of flow.

These occurrences are observed from smoke stacks or chimneys that release pollutants such as sulphur dioxide into the atmosphere creating unfavourable weather and climate conditions. The mean motion of emissions from smoke stacks and chimneys was studied by Briggs (1969). Morton (1959) studied the rise height of plumes created from industrial chimneys to predict the spread of pollutants in the atmosphere as they are affected by the ambient stratification, the effective decrease in density with height.

The puff from cigarette smoke that creates a well defined plume breaks up into small eddies far from their source. Volcanic eruptions that release hot vaporized gases and particles into the atmosphere create both long- and short-term environmental effects on surrounding agriculture, human health and global climate (Zielinski, 2002; Robock, 2004). An example of such eruption

is the most recent Mount Sinabung volcanic eruption in Indonesia on February 3, 2014 and others that include fire plumes are used to design smoke detectors and sprinklers (Joseph and Vincent, 2003; Heskestad, 2014).

The discharge of fluid such as contaminants into rivers from outfalls spreads vertically and transversely as it mixes through turbulence created naturally can behave buoyancy-driven and hence plume-like. Sewage created from ocean outfalls has been studied by Brooks and Koh (1965) and Fan (1967). Brooks and Koh (1965) predicted the behaviour of the effluent generated by sewage jets from a diffuser into the stratified ocean. From experiments, Fan (1967) analyzed the dynamics of inclined buoyant jets in stagnant stratified environments.

In the literature plumes are distinguished based on their source and environmental conditions. They are further categorized based on the dynamics and characteristics of their structure such as the magnitude of the volume, momentum and buoyancy fluxes, Reynolds number of the flow and the direction of buoyancy relative to momentum fluxes. The following section will discuss the classification of plumes based upon these characteristics.

1.1   Categorizing plumes

Figure 1.1 gives a summary of the classification of plumes used in the fluid dynamics literature. Plumes are formed from laminar or turbulent flows at their sources with low or high Reynolds number respectively. Laminar plumes can grow unstably in time and consequently become turbulent far from their sources. Beyond it neutral buoyancy level, the vertical velocity of the plume decreases as moves upwards away from the source. Experiments of laminar plumes were investigated by Gerbhart et al. (1970) and Mollendorf

and Gerbhart (1973). Using the Boussinesq approximation they showed a simplification of the conservation equations of momentum, mass and energy in which they obtained the governing partial differential equations that were further extended and discretized for numerical purposes. Turbulent plumes are created from the entrainment of ambient fluid across its boundary with turbulent eddies that enhance mixing. Plumes created from a line or an effective point source that become turbulent in nature form an intrusion that results in a planar flow with a straight front or an axisymmetric flow with a circular front in a stratified ambient fluid (Didden and Maxworthy, 1982).

The flows from a source of excessive initial momentum flux are called either forced plumes or buoyant jets that become buoyantly driven far from their sources. Buoyant jets were studied by Robi (1982) and others outlined in Section 1.2. Pure plumes are only driven by buoyancy forces and have zero momentum flux (M_0=0). The influence of the volume flux, Q_0, momentum flux, M_0, and buoyancy flux, F_0, when non-zero at the source is expressed through the non-dimensional parameter, Γ_0, defined by Morton (1959) as

$$\Gamma_0 = \frac{5 Q_0^2 F_0}{4 \alpha \pi^{1/2} M_0^{5/2}}, \tag{1.1}$$

in which α is the entrainment constant (see Appendix A) and Γ_0 is a constant where $0 < \Gamma_0 < 1$ for forced turbulent plumes, $\Gamma_0 = 1$ for pure plumes with the same momentum and volume fluxes and $\Gamma_0 > 1$ for lazy plume created from a source of deficiency in momentum flux.

If the momentum and buoyancy fluxes are directed in the same direction the plume is called a positively buoyant plume. If the momentum and buoyancy fluxes are oriented in opposite direction the plume is called a negatively buoyant plume or fountain.
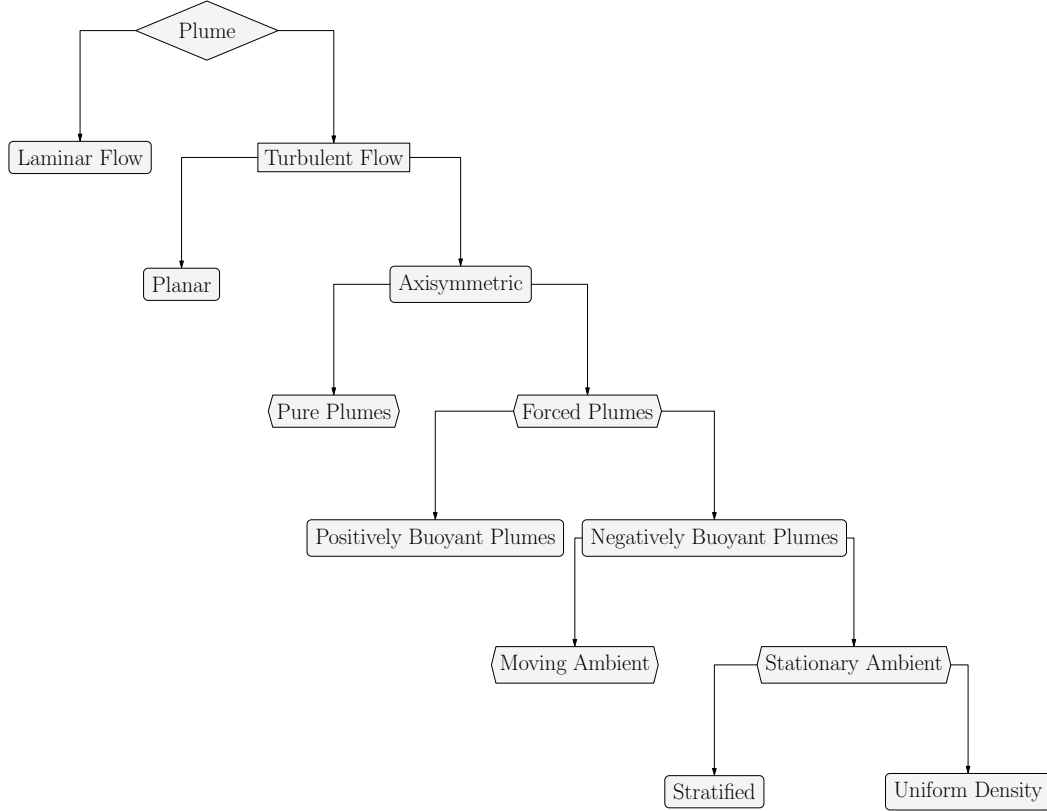
Figure 1.1: Diagram shows the categories of plumes.

The environment in which such plumes are created is either stationary or moving at some horizontal mean speed. In which case the ambient or environment could be uniform or stratified.

The atmosphere and ocean are stratified due to non-uniform temperature and/or salinity. In a stably stratified liquid, density decreases with height as

$$\frac{d\bar{\rho}}{dz} < 0, \tag{1.2}$$

where $\bar{\rho}(z)$ is the density of the ambient fluid as a function of height, z.

In stably stratified liquid, the square of the buoyancy frequency is given

by

$$N^2 = -\frac{g}{\rho_{00}}\frac{d\bar{\rho}}{dz}, \tag{1.3}$$

which is the frequency of the oscillatory motion of a fluid in a stratified ambient where g is the gravitational acceleration and ρ_{00} is the characteristic density.

In stably stratified gas, the potential temperature increases with height as

$$\frac{d\bar{\theta}}{dz} > 0. \tag{1.4}$$

where $\bar{\theta}(z)$ is the ambient potential temperature. Explicitly, the potential temperature is given by

$$\bar{\theta} = T(z)\left(\frac{P_{00}}{\bar{P}(z)}\right)^{\kappa} \tag{1.5}$$

where $\kappa = 2/7$ is a constant, $T(z)$ and $\bar{P}(z)$ are the ambient temperature and pressure, respectively. In stably stratified gases the square of the buoyancy frequency is given in the Boussinesq approximation by

$$N^2 = \frac{g}{\theta_{00}}\frac{d\bar{\theta}}{dz}, \tag{1.6}$$

where θ_{00} is the characteristic potential temperature.

In uniformly stratified environments $N^2 > 0$ and is constant. In uniform environments $N^2 = 0$. This research will examine well-mixed turbulent forced plumes with high Reynolds number in stationary and uniformly stratified environments.

1.2 Literature Review

The understanding of statistically steady turbulent forced plumes in uniform and uniformly stratified environments begins with the work of Morton et al. (1956), who derived equations for the evolution of volume, momentum and buoyancy fluxes in a plume assuming that the lateral entrainment of the ambient into the plume at a particular height was proportional to the vertical speed of the plume at that height. Although highly successful in predicting the evolution of forced plumes in a uniform ambient, the predictions failed to predict the full evolution of a negatively buoyant plume because the entrainment assumption inaccurately captured the dynamics at the fountain top and the consequent lateral entrainment of the descending fluid surrounding the plume core (McDougall, 1981; Bloomfield and Kerr, 2000).

From the entrainment interaction between the upward and descending turbulent flows, Morton (1962) and McDougall (1981) developed a semi-empirical theoretical model of the evolution for a negative buoyant jet created from an upward vertical injection of dense fluid into a homogeneous environment. These equations predicted the width, vertical velocity, final height and buoyancy for the upward and downward flows of the fountain.

Nonetheless, a scaling analysis reveals how the height of a fountain depends upon the momentum and buoyancy fluxes at the source (Morton, 1962; Turner, 1966). Turner (1966) conducted a series of experiments to show that the interaction between the upward and downward flows of a plume acts to reduce its maximum height. The maximum height of the plume is reduced to a lower steady state height from turbulent exchange between the upward and downward flows as buoyancy acts on the heavier collapsing fluid (downward flow). Using dimensional arguments, Turner (1966) showed that the maximum height, Z_{m}, was related to the ambient stratification, source momentum

and buoyancy fluxes as $Z_{\mathrm{m}} \propto M_0^{1/4} N^{3/4}$ and $Z_{\mathrm{m}} \propto F_0^{1/4} N^{1/2}$ respectively.

The work of Morton et al. (1956) was extended to investigate forced plumes in uniform and stratified environments (Morton, 1959). Through theory he showed that forced plumes created from a source of finite size which delivers mass, momentum and buoyancy is related to the flow from a virtual point source of only buoyancy and momentum fluxes.

Through theory and experiments of fountains in uniform stratification, Bloomfield and Kerr (1998, 2000) examined the maximum and steady state rise height as well as the height at which the intrusion spreads. The theory which assumed that momentum dominated over negative buoyancy at the plume source, provided good semi-empirical predictions of the spread height in this regime. Theirs was the only experimental study that examined the spread height of turbulent fountains in a uniformly stratified environment.

Most theoretical and experimental studies of the radial spread of an intrusion in stratified fluid neglect the dynamics of the plume and collapsing fountain. Instead, they assume a constant horizontal flux of volume, momentum and buoyancy from a localized source (Maxworthy, 1972; Huppert and Simpson, 1980; Didden and Maxworthy, 1982; Ivey and Blake, 1985; Kotsovinos, 2000; Devenish and Rooney, 2014). Assuming that the volume flux and intrusion height are constant and that the evolution is self-similar, the radius of the intrusion front is predicted to increase in time as $R_f \propto t^{2/3}$ (Huppert and Simpson, 1980). Taking into account the ambient stratification, Kotsovinos (2000) instead predicted $R_f \propto t^{3/4}$.

More recently, Ansong and Sutherland (2010) studied internal waves generated by convective plumes with applications to storm top impinging upon the stratosphere and deep oceanic convection. Although the study was not focused on predicting the radial spread of the intrusive gravity current in

the umbrella region, they found the relationship, $R_{\mathrm{f}} \propto t^{3/4}$, for the intrusion spread in the buoyancy-inertia regime.

From a theoretical perspective, Devenish and Rooney (2014) recently analyzed the plume rise and spread in a stably stratified moving and stationary environments. They investigated the radial intrusion at its neutral buoyancy level during and after transition in the buoyancy-inertia regime. This led to the equations that predicted the radius, speed and thickness of the intrusion at its neutral buoyancy level.

There are relatively few studies examining the radial advance of an intrusion resulting from the collapse of a plume in uniformly stratified fluid some of which are reviewed and presented by Kaye (2008).

The above theoretical and experimental work on jets, plumes and fountains in stratified and uniform environments have considered the application of the Boussinesq approximation in which the density difference between the source and ambient fluid is relatively small with an upper bound of $|\Delta\rho|/||\bar{\rho}|| \approx 0.1$ (Crapper and Baines, 1976).

This research aims to use experiments to study the dynamics of radial intrusions emanating from Boussinesq and non-Boussinesq turbulent plumes at their neutral buoyancy levels in a stratified ambient fluid for which $|\Delta\rho|/||\bar{\rho}|| \gtrsim 0.1$. We present the experimental results with applications to volcanic ash cloud created from a forced turbulent volcanic plume spreading at their neutral buoyancy level in the stratosphere and the accidental discharge of oil into the ocean even though their dynamics maybe different.

1.3 Motivation

Turbulent plumes in uniformly stratified ambient fluids have three prominent regions of interest: a convective, a gas-thrust and a radial spreading region. Plumes are widely studied because of their local environmental impacts in volcanic eruptions and emissions from industrial chimneys or smoke stacks (see Section 1).

Although turbulent plumes have been studied for over six decades, their dynamics are still not well understood as the demand for more sophisticated analyses and experimental designs are required to make predictions from experimental observations that sufficiently captures the dynamics of the plume spread. An example of such is the radial spread of an intrusion emanating from the plume centerline at its neutral buoyancy level in a uniformly stratified ambient. Its front position is expected to follow the power law relationship, $R_f \sim t^P$ where 'p' is the theoretically or experimentally determined exponent. Different values for this exponent have been predicted creating uncertainty (Kotsovinos, 2000) for which power law correctly predicts the intrusion spread particularly in the buoyancy-inertia regime (see Table 3.2). The correct prediction of the time-dependent radial spreading intrusion emanating from a forced turbulent plume at its neutral buoyancy level in a stratified ambient fluid can be extended to understand the dynamics of volcanic ash cloud spreading at early time shortly after it collapses in the stratosphere.

In addition, the intrusion thickness as a function of radial spread in time is not well known as there are relatively few studies on this aspect of the plume. Shallow water theory of an intrusive gravity current in uniformly stratified ambient fluid predicts that the intrusion thickness evolves only in time (Ungarish, 2009). Our experiments of radial spreading intrusion created from a forced turbulent plume in a uniformly stratified fluids will investigate

the intrusion thickness as a function of time and position to test the validity of this assumption. This may be used to understand how the height of a volcanic ash cloud spreading in the stratosphere vary as it is difficult to collect in situ data in such circumstances (see Section 1.3.1).

Finally, the factors that determine the spread height of the plume in a stably stratified ambient fluid are not well understood as the plume becomes momentum- or buoyancy-dominated. Many researchers have studied the maximum penetration height of the plume (List, 1979; Morton et al., 1956; Bloomfield and Kerr, 1998, 1999; Turner, 1966; Caulfield and Woods, 1995; Fox, 1970), but very few have extended their study to the plume spreading height (Caulfield and Woods, 1992). This research aims to examine the factors that influence the spreading height of a turbulent plume in a stratified environment.

1.3.1   Supervolcanoes in the stratosphere

Volcanic eruptions cause the discharge of hot volcanic gases and particles that can penetrate vertically into the atmosphere up to tens of kilometers. Such eruptions have a convective column of three distinct regimes (Costa et al., 2010): a gas thrust or jet region, an intermediate convective region and an upper umbrella region as shown in Figure 1.2. In the jet region, the effluent from the volcano rises primarily due to momentum. This region occurs over a small fraction of the total eruption column height. In the ensuing intermediate convective region, as the flow entrains ambient moisture-laden air it becomes controlled primarily by buoyancy forces.

In the stratified atmosphere, the momentum and buoyancy fluxes decrease as the plume becomes relatively more dense until it becomes negatively buoyant and ultimately reaches a terminal point called its maximum height where

10

the momentum flux becomes zero. The plume then collapses upon itself as a fountain falling downward about the central rising plume until it reaches its neutral buoyancy level where the fluid originating from the plume has the same density as the surrounding ambient. From there it spreads radially outwards as an intrusive gravity current forming an umbrella region.

For large volcanic eruptions, the influence of ambient winds can be ignored during the development of these three regimes as the speed of the initial rising plume exceeds stratospheric wind speed while at its maximum height $(w(Z_m)=0)$, the buoyancy exceeds the effects of ambient wind speed. The plume collapse and initial horizontal spread at its neutral buoyancy level remains unaffected by stratospheric winds. Hence, within the first few hours of spread the umbrella cloud region is approximately symmetric in shape (Baines and Sparks, 2005; Costa et al., 2013) as it spreads within the buoyancy-inertia regime. The effects of the Earth rotation during the plume rise and spread within the buoyancy-inertia regime is also ignored as the time taken for the plume to rise in the stratosphere (typically 1 hr) is shorter than the Earth's inertial period (approximately 10 hr). Because our experiments neglect winds and rotation and because there are ample observations we have chosen to apply our results to the large Mount Pinatubo eruption. Beyond the buoyancy-inertia regime the speed of the spreading umbrella cloud decreases under the influence of viscosity effects while the cloud is advected away from the plume origin by ambient stratospheric winds (Helfrich and Batisti, 1991).

Volcanic particles vary in size by several orders of magnitude, ranging from very fine submicron ash to particles larger than 1 m in diameter (Sparks et al., 1997). Larger particles leave the eruption column at lower levels while finer ash particles in the umbrella region can remain in the stratosphere for several days while spreading over the entire atmosphere. The spread of these

particles can damage airplane engines (Williams and Thomas, 2011) and can cause short-term but non-local cooling effects on climate (Costa et al., 2006; Robock, 2004) as relatively small amount of finer ash particles suspended in the atmosphere are dispersed by high stratospheric winds. The fall out of these particles from the eruption column has increased the effects of human respiratory problems and has extensively destroy agriculture and severely damage many homes (Costa et al., 2006; Robock, 2004).

Although simulations model the passive advection of particles by the synoptic scale winds (Holasek et al., 1995), less well understood are the dynamics of the eruption column and the intrusion that emanates horizontally in its vicinity. The entrainment of moist air, the release of heat internally by particles, the rate of supplied volume flux and non-Boussinesq effects applied near the source of the eruption column are additional sources that provide buoyancy in the plume rise and spread (Wilson et al., 1978; Holasek et al., 1996a; Sparks et al., 1986). Turbulence, high temperatures and particles make it difficult to collect in situ data within the rising plume and its radial spreading region (Textor et al., 2006). Likewise, the dynamics are too complex to be captured by direct numerical simulations. Nonetheless, insights have been gained through approximate theories (Woods, 2010) guided by the results of laboratory experiments (Woods, 2010).

1.3.2   Dynamics of Supervolcanoes

To understand the dynamics of large volcanic eruptions in the stratosphere, it is useful to appreciate the properties of this stratified ambient region that lies immediately above the tropopause. In the atmosphere temperature varies with vertical height. Within the first $8-16$ km above the Earth's surface, temperature decreases with height at approximately $10°C/$ km (temperature

Umbrella
cloud

Radial spreading level

Convective
region

Ambient
Entrainment

Gas -Thrust
region

virtual origin

vent
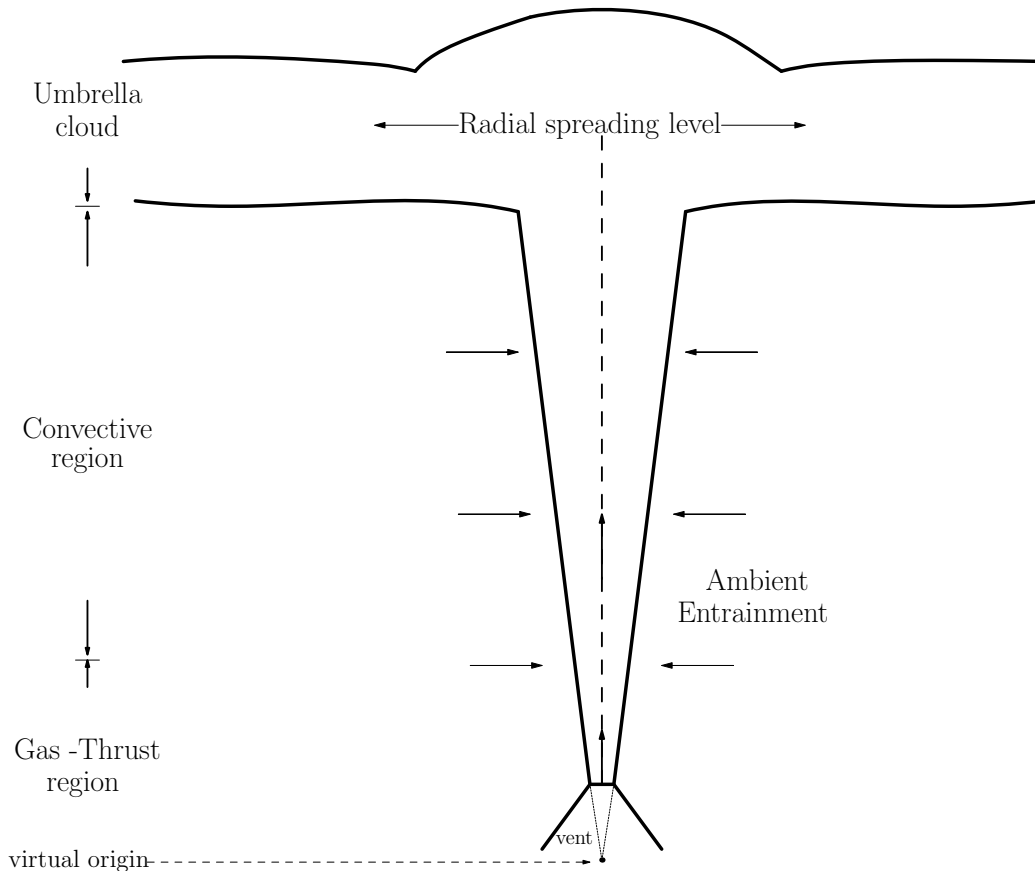
Figure 1.2: Schematic diagram of a volcanic eruption released from an isolated hot spot into the atmosphere creating three distinct regions called the gas-thrust, convective and umbrella cloud regimes.

lapse rate) in this lower region called the troposphere.

Immediately above this region is the tropopause that separates the troposphere and stratosphere. Above the tropopause, the temperature decreases less quickly with and even increases with height in a region called the stratosphere that extends up to approximately 50 km. The increase in temperature within the stratosphere is due to the absorption of ultraviolet (UV) solar radiation by the atmospheric ozone.

In the atmosphere, to a close approximation the upward ambient pressure gradient is balanced by the downward gravitational force acting on surround-

13

ing air parcels is given by

$$\frac{d\bar{P}}{dz} = -\bar{\rho}g, \tag{1.7}$$

where $\bar{P}$ is the atmospheric pressure that changes with altitude z, g is the gravitational acceleration and $\bar{\rho}$ is the ambient density. Equation 1.7 is called the hydrostatic balance equation.

The region of our interest is the stratosphere, which has an approximately constant stratification. The release of hot volcanic gases and particles into the atmosphere moves vertically upwards with the entrainment of air and moisture. The entrainment of ambient air and moisture that gain sufficient heat energy through the heat transfer from hot pyroclastic materials (such as hot particles and gases released) inside the plume will expand and increase in volume (Woods, 1988). As a result, the temperature of the rising volcanic plume decreases. The continuous entrainment of ambient fluid cause the temperature of the rising plume column to decrease substantially over large vertical distances resulting in non-Boussinesq effects. If there is sufficient internal heat and energy this will create a mixture that becomes buoyant after sufficient ambient is entrained (Woods, 1988). Such eruptions may rise vertically over tens of kilometers in the atmosphere as it becomes buoyancy-driven.

1.3.3 2010 Deepwater Horizon Oil Spill

Other natural occurrences of plumes in stratified fluid include the accidental discharge of oil from a deep underground reservoir into a large body of water such as the ocean. In particular, we consider the 2010 Deepwater Horizon oil spill that has caused ecological, economical, environmental and health damage (Frias-Torres et al., 2011). The accidental discharge of oil may be as a result

of damaged pipelines, submerging tankers and/or oil blowouts. The most difficult, destructive and harmful of the three is oil blowout (Yapa and Chen, 2004). Oil blowout is caused from the drilling of an area of uncontrollable high pressure fluid (oil, gas or water) that can spread unstoppably in the ocean where its point of release is from a small crack.

The accidental discharge of oil from such an underground drilling site creates a mechanism which behaves similar to a jet-like flow that transforms into a plume-like flow closer to the surface of the ocean. However, there are other dynamics such as gas bubbles, oil droplets and gas hydrates that may crucially affect the dynamics of the plume. In stratified environments, gas bubbles can continuously rise beyond the predicted rise height of a fountain and spread horizontally (McDougall, 1978; Woods, 2010).

1.4   Thesis Organization

Chapter 2 reviews the theory for the rise and spread of a forced turbulent plume in a stratified ambient fluid. The prediction for the spread height of Bloomfield and Kerr (1998) is extended to include the influence of plumes dominated by buoyancy instead of momentum at their sources as they are influenced by the ambient stratification. Even though such plumes are initially driven by momentum. This is followed by presentation of two models that predict the radial spread of the intrusion emanating from a forced plume in uniformly stratified ambient fluid. The general scaling analysis used to derive the model $R_{\rm f} \sim t^{3/4}$ is presented in the Appendix B along with a separate derivation of the two models given by Devenish and Rooney (2014). (The governing equations for the momentum, buoyancy and volume fluxes are explicitly derived from first principles in Appendix A). The experimental set-up

and analysis are described in Section 3.2.

Chapter 3 presents the qualitative observations, quantitative analysis and results describing the radial advance and structure of the intrusion as it spreads at its neutral buoyancy level in a uniformly stratified ambient fluid. The material presented in this chapter, is published in the *Physics of Fluids*, Vol. 26 pp. $036602-1--17$.

Chapter 4 presents the experimental results of the spread and maximum depths of the plume and the intrusion emanating from the plume centreline at its neutral buoyancy level in a uniformly stratified ambient fluid.

In Chapter 5 the experimental results are compared to observations of large volcanic plumes penetrating into and spreading within the stratosphere. Application to the 2010 Gulf of Mexico Deepwater Horizon oil spill is also examined. A section of the experimental results presented in this chapter is also is published in the *Physics ofFluids*, Vol. 26 pp. $036602-1--17$.

Chapter 6 gives the summary and conclusion of this research work. This chapter also discusses the possible future work that can be used to extend this body of work presented on forced turbulent plumes in uniformly stratified fluids.

Chapter 2

Theory

2.1 Introduction

This chapter derives the equations associated with the flow of a forced turbulent plume in a uniformly stratified ambient fluid. The dynamics of a forced plume in uniform and in uniformly stratified fluids is presented in Section 2.2 which also describes the evolution of such plumes. The prediction for the spread height of Bloomfield and Kerr (1998) is also extended in this section to include the influence of forced plumes dominated by buoyancy instead of momentum at their sources as they are influenced by the ambient stratification. The equations that predict the radial spread of an axisymmetric intrusion front position in time at its neutral buoyancy level are explicitly derived in Section 2.3. Other detailed derivations that use scaling analysis to predict the radial spread in time are given in Appendix B along with a separate derivation of the two models that predicts the radial spread in time by Devenish and Rooney (2014).

2.2 Plumes in a Stratified Environment

Although the motivation for this work is the examination of volcanic plume rise and spread in the stratosphere, it is convenient in laboratory experiments to examine a dense descending plume in uniformly stratified fluids. In the Boussinesq approximation, this circumstance is equivalent to a rising plume of less dense fluid with positive buoyancy. In reality, the density of the eruption column near the source can be vastly different from the surrounding ambient and the column itself propagates over more than one density scale height (about $8\,\mathrm{km}$) as it passes into the stratosphere. Thus non-Boussinesq effects would play an important role in determining the plume rise. However, our focus here is upon the transition of the plume into a collapsing fountain and the consequent radial spreading intrusion. These dynamics occur over a relatively small vertical distance within the stratosphere (Sparks et al., 1986; Baines and Sparks, 2005), so that the Boussinesq approximation is reasonably applied. For simplicity in this study, we do not include particles within the plume, focusing instead upon the influence of buoyancy and inertia of the fluid associated with the plume and the radial intrusion.

The theory presented here is for a turbulent forced plum that initially moves downward into a uniformly stratified fluid, and is also consistent with our experimental setup, as illustrated schematically in Figure 2.1 where O represents the centreline of the rising plume column. Fluid of density, ρ_0, greater than the surrounding ambient density ($\rho_0 > \rho_{00} = \bar{\rho}(Z{=}0)$) at the nozzle depth, is injected downward with volume flow rate, Q_0, from a source of radius, b_0. This falls to a maximum depth, Z_m, then rises as a fountain and finally spreads radially outwards at its neutral buoyancy level given by the spreading depth, Z_s. The radius of the incident plume at Z_s, is denoted by R_0. The radius at which the intrusion is first observed to propagate radially in the

a) Front view of experiment setup
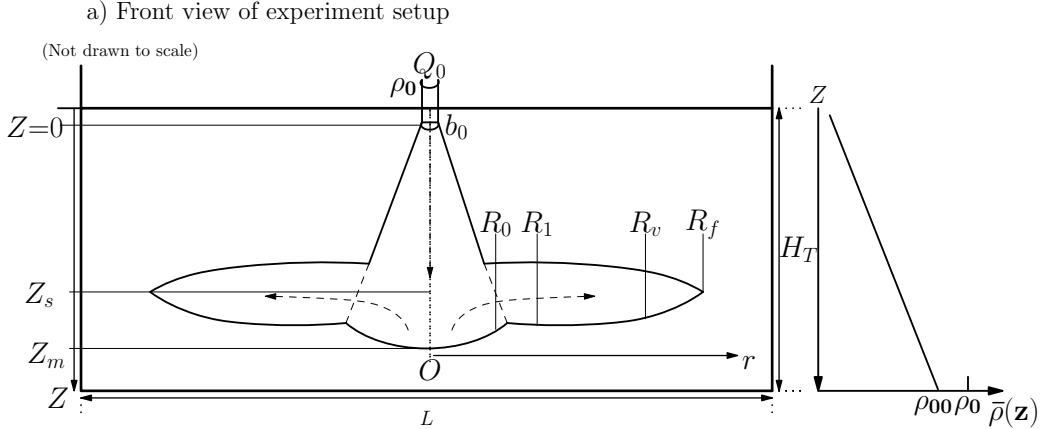
Figure 2.1: Side-view of a dense plume falling and spreading in a uniformly stratified environment not drawn to scale.

inertia-buoyancy regime is denoted by R_1 estimated by Devenish and Rooney (2014) to be approximately $3R_0$. The intrusion front position increases in time is denoted by $R_f(t)$. Beyond a radius, R_v, the advance of the intrusion is dominantly influenced by a balance of viscosity and inertia.

Sections 2.2.1-2.2.2 describe the dynamics of forced turbulent plumes in uniform and uniformly stratified fluids that initially behave jet-like at the source then become plume-like far above the source. Section 2.2.3 discusses the evolution of a turbulent forced plume as it transforms into a fountain when rising in a uniformly stratified ambient. Section 2.2.4 describes the stratification associated with the background fluid. The factors that determine and set the spreading depth, Z_s, of a forced plume are outlined in Section 2.2.5.

2.2.1 Forced Plume in Uniform Ambient

Forced plumes are created from a source of both momentum and buoyancy but having excessive momentum (Morton, 1959). Forced plumes are also referred to as buoyant jets simply because they exhibit both jet and plume dynamics as a free turbulent shear flow (Brooks, 1972; Ansong and Sutherland, 2010). In a stratified ambient, a jet rising from an effective point source is controlled

19

by its initial momentum flux near the source with negligible buoyancy then transforms into a pure plume that is controlled by buoyancy forces far from the source. The continuous entrainment of ambient fluid into the vertically rising plume causes its buoyancy flux to decrease towards its neutral buoyancy level.

The characteristics of a turbulent forced plume created from an effective point source are determined by the source momentum and buoyancy fluxes, given respectively by

$$M_0 = \pi b_0^2 w_0^2 = \frac{Q_0^2}{\pi b_0^2} \tag{2.1}$$

and

$$F_0 = \pi b_0^2 w_0 g_0' = Q_0 g_0'. \tag{2.2}$$

Here w_0 is the mean vertical velocity at the source,

$$w_0 = \frac{Q_0}{\pi b_0{}^2}, \tag{2.3}$$

and g_0' is the reduced gravity at the source:

$$g_0' = g\,\frac{\rho_0 - \rho_{00}}{\rho_{00}}, \tag{2.4}$$

in which g is gravity and $\rho_{00}=\bar{\rho}(Z{=}0)$ is the density of the ambient fluid at the nozzle, as shown in Figure 2.1. The definitions of w_0 and g_0' are such that F_0 is always positive, consistent with the understanding that buoyancy initially acts in the same direction at which the fluid is injected. The dimensions of the fluxes at the source: Q_0, M_0 and F_0 correspond in cgs units are cm^3/s, cm^4/s^2 and cm^4/s^3 respectively.

The Froude number at the source is

$$\text{Fr}_0 = \frac{w_0}{\sqrt{b_0 g_0'}}. \tag{2.5}$$

The Reynolds number at the source is

$$\text{Re}_0 = \frac{w_0 b_0}{\nu}, \tag{2.6}$$

in which ν is the kinematic viscosity of the fluid. For fresh and salt water, $\nu \simeq 0.01$ cm^2/s. If Re_0 is sufficiently large, the plume flow is turbulent and viscosity plays a negligible role at least insofar as entrainment, momentum and buoyancy transport are concerned.

2.2.2 Jet Length

A dense fluid injected vertically downwards into a uniformly stratified ambient fluid will move away from the source as it is initially driven by momentum. After some time and distance from the source buoyancy will begin to dominate the flow until it becomes buoyant or plume-like, the vertical distance at which this occurs being called the "jet length".

From M_0 and F_0, dimensional arguments reveal the jet length scale of the system (Turner, 1966),

$$H_{\text{p}} = M_0^{3/4} |F_0|^{-1/2}. \tag{2.7}$$

For distances larger than H_{p}, buoyancy dominates the momentum associated with the vertical flow at the source (see Figure 2.2) .

The corresponding time for fluid leaving the nozzle to pass through this transition from a momentum-driven flow to a buoyancy-driven flow is Chen
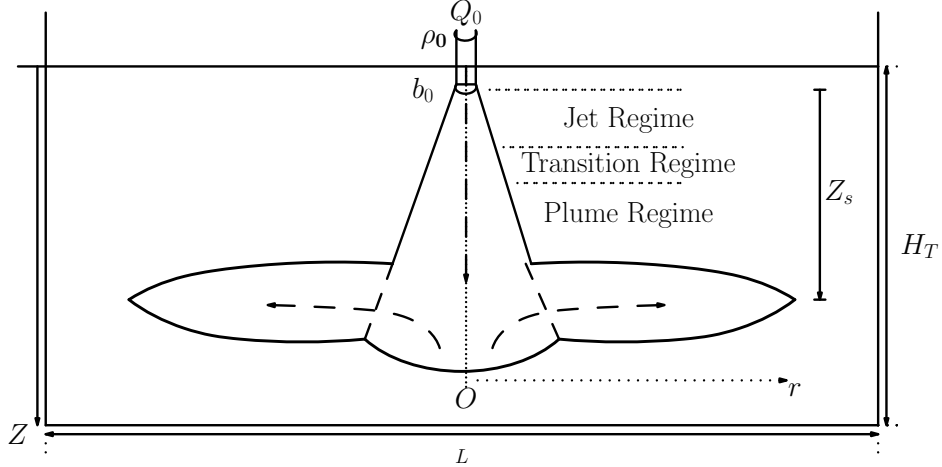
Figure 2.2: Side-view of a dense plume falling to a maximum depth where it then collapses to and spreads at its neutral buoyancy level in a uniformly stratified environment showing its jet regime (momentum-driven), transition regime (from jet- to plume-like flow) and plume regime (buoyancy-driven).

(1980)

$$t_p = \frac{M_0}{|F_0|}. \tag{2.8}$$

2.2.3 Fountain in Uniform Ambient

In a uniform ambient fluid, if F_0 and M_0 have the same sign, H_p, determines the transition from jet-like (momentum-driven flow) to plume-like (buoyancy-driven flow) behaviour in a forced plume. However, if F_0 and M_0 have opposing signs, H_p is a measure of the rise height of a "forced fountain" (Turner, 1966; Burridge and Hunt, 2012). Fountains were first studied by Priestley and Ball (1955), Morton (1959) and Abraham (1967).

A fountain or a negatively buoyant plume is created from the continuous injection of fluid descending into a more dense ambient. This is equivalent to the continuous upward injection of fluid into a less dense ambient. In both cases, the buoyancy opposes the momentum of the flow upon rising to a

maximum vertical distance where its momentum flux goes to zero. The flow then collapses and falls back upon itself to its neutral buoyancy level.

In a uniformly stratified fluid, a forced plume injected into a stratified ambient will eventually overshoot its neutral buoyancy level and so transform into a fountain which rises to a maximum height where its momentum flux goes to zero and then collapses, ultimately the returning fluid reaches its neutral buoyancy level from which it then spreads radially.

Through experiments of a dense fluid injected vertical upwards into an ambient of fresh water using dimensional arguments Turner (1966) showed that the maximum penetration height of a fountain is given by

$$Z_{\mathrm{m}} = C_f H_{\mathrm{p}}, \tag{2.9}$$

where the empirically determined constant, C_f, was found to be 2.46.

2.2.4 Buoyancy Frequency

The maximum rise height and the consequent height of a radially spreading intrusion depend not only upon H_{p}, but also upon the ambient stratification expressed through the buoyancy frequency, N. In salt-stratified Boussinesq fluid, N is given by

$$N = \sqrt{-\frac{g}{\rho_{00}} \frac{d\bar{\rho}}{dz}}, \tag{2.10}$$

in which $\bar{\rho}(z)$ is the ambient density. If $\bar{\rho}$ decreases linearly with height then N is constant and the fluid is said to be uniformly stratified.

Unlike plumes created from salt-stratified and uniformly dense environments where the density difference between the source and ambient is critical, for large volcanic eruption columns spreading in the stratosphere, it is the potential temperature that is important. In the atmosphere the buoyancy

frequency is given by

$$N = \sqrt{\frac{g}{\bar{\theta}} \frac{d\bar{\theta}}{dz}}, \tag{2.11}$$

where $\bar{\theta}(z)$ is the potential temperature that increases with height in a stably stratified gas. In the Boussinesq approximation $\bar{\theta} \approx \theta_{00}$ in the denominator within the square-root of (2.11).

2.2.5 Maximum and Spreading Depth in Uniformly Stratified Ambient

The relative influence of the ambient stratification is expressed through the non-dimensional parameter, σ, defined by List (1979); Bloomfield and Kerr (2000, 1998):

$$\sigma \equiv \frac{M_0{}^2 N^2}{F_0{}^2} = t_p^2 N^2. \tag{2.12}$$

The square-root of σ is a measure of the time-scale, t_p, for plume rise over the jet length relative to the buoyancy period. If σ is large, the flow from the source remains jet-like when stratification becomes important. If σ is small, the flow is plume-like when stratification becomes important.

Experiments of fountains in uniformly dense and stratified fluids show that they first reach a maximum height before falling back toward the source. Thereafter, the fountain top fluctuates about a steady state height, Z_{m}, moderately smaller than the initial maximum height, Z_{fm} as shown in Figure 2.3 (Turner, 1966; Bloomfield and Kerr, 1998; Ansong and Sutherland, 2010). From Z_{fm} the plume then collapses to its neutral buoyancy level spreading radially outwards at its spreading depth, Z_{s}. In experiments we have not investigated the maximum depth, Z_{fm}, but have analyzed the maximum steady state and spreading depths, Z_{m} and Z_{s} respectively. The steady state maximum depth was found from the average of the vertical oscillatory motion of
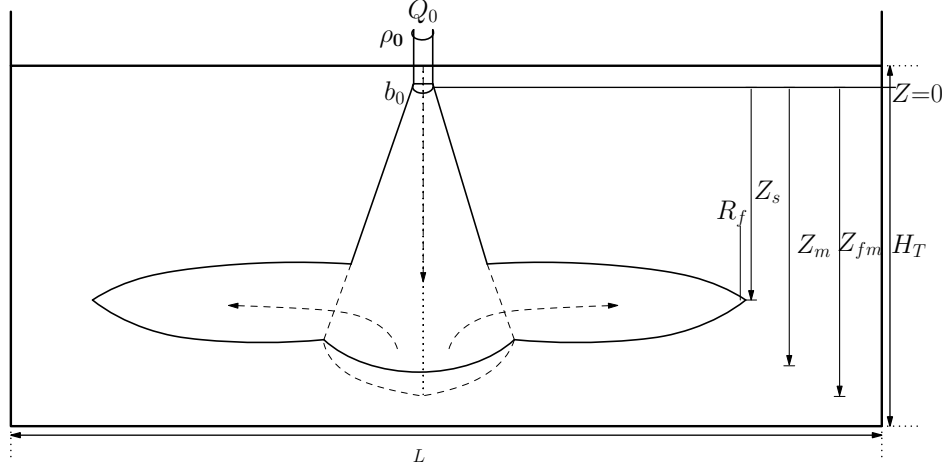
Figure 2.3: Side-view schematic of plume shows the spreading depth, Z_{s}, maximum penetration depth, Z_{fm} and the steady state depth, Z_{m}.

the plume top in time.

The spreading height, Z_{s}, of the radial intrusion is expected to scale with its maximum steady state height, Z_{m}. In their experiments of negatively buoyant fluid injected upwards into uniformly stratified fluid, Bloomfield and Kerr (1998) found the scaling, $Z_{\mathrm{s}}/Z_{\mathrm{m}} \sim 0.51$. Here we examine how this relationship varies if the buoyancy flux, F_0, at the source is of the same sign as the momentum flux, M_0.

Just as Z_{m} should depend upon M_0, F_0 and N (or, equivalently, H_p and σ), so should the spread height, Z_{s}, of the radial intrusion. Both Z_{m} and Z_{s} can be estimated through numerical integration of the equations for a turbulent forced plume with constant entrainment proportional to the vertical speed at the plume centre (Morton, 1959; Ansong and Sutherland, 2010). Here we consider the asymptotic limits of buoyancy-dominated and momentum-dominated sources.

Following Bloomfield and Kerr (1998), we write the formula for the spread height as

$$Z_{\mathrm{s}} = f(\sigma)H_{\mathrm{p}}, \tag{2.13}$$

25

for some function, $f(\sigma)$. If $\sigma \ll 1$, stratification acts upon a buoyancy-driven flows. This implies that Z_s should be independent of M_0. Combining (2.7) and (2.12) so as to eliminate M_0 on the right-hand side of (2.13) gives the scaling relationship,

$$f(\sigma) \propto \sigma^{-3/8} \Rightarrow Z_\mathrm{s} \propto F_0^{1/4} N^{-3/4}. \tag{2.14}$$

Likewise, if $\sigma \gg 1$, stratification acts upon a momentum-driven flow, and so Z_s should be independent of F_0. Eliminating F_0 on the right-hand side of (2.13) gives the scaling relationship,

$$f(\sigma) \propto \sigma^{-1/4} \Rightarrow Z_\mathrm{s} \propto M_0^{1/4} N^{-1/2}. \tag{2.15}$$

The second of these limits was derived by Bloomfield and Kerr (1998), who explicitly found through laboratory experiments that

$$f(\sigma) = 1.53\,(\pm 0.10)\,\sigma^{-1/4}, \quad \text{for} \ \ \sigma \gtrsim 100. \tag{2.16}$$

Their experiments were designed to study fountains in stratified fluid for which the source momentum and buoyancy fluxes were opposite signed as such, they were unable to explore the case of small σ because the fountain would spread right at the source when the momentum flux was too small to overcome buoyancy at the source. However, our study of a forced plume source is designed to access both small and large σ limits.

These limits have been explored previously (List, 1979) in experiments separately examining jet-like sources (Fan, 1967; Fox, 1970) and plume-like sources (List, 1979; Morton et al., 1956; Caulfield and Woods, 1995).

A theoretical study supported by a few experiments was conducted by List

(1979) to determine the factors that set the maximum depth (also referred to as the terminal depth) of a buoyant jet falling in a linearly stratified ambient. They found through a small number of experiments (recast in the notation of this thesis) that $Z_{\mathrm{m}} \simeq 3.8 F_0^{1/4} N^{-3/4}$ ($Z_{\mathrm{m}}/H_{\mathrm{p}}$=3.8 ($\pm 0.2)\sigma^{-3/8}$) for $\sigma \ll 1$ and $Z_{\mathrm{m}} \simeq 1.43 M_0^{1/4} N^{-1/2}$ ($Z_{\mathrm{m}}/H_{\mathrm{p}}$=3.8 ($\pm 0.2)\sigma^{-1/4}$) for $\sigma \gg 1$. This showed agreement with their corresponding theoretical power law predictions.

A section of the work of Morton et al. (1956) also showed the dependence of the fluxes at the source on the maximum penetration height of a turbulent plume in a uniformly stratified ambient fluid. Morton et al. (1956) experiments showed that $Z_{\mathrm{m}} \simeq 5.75 F_0^{1/4} N^{-3/4}$ ($Z_{\mathrm{m}}/H_{\mathrm{p}} \simeq 5.75 \sigma^{-3/8}$) for $\sigma \ll 1$ and $Z_{\mathrm{m}} \simeq 1.43 M_0^{1/4} N^{-1/2}$ ($Z_{\mathrm{m}}/H_{\mathrm{p}} \simeq 1.43 \sigma^{-1/4}$) for $\sigma \gg 1$ outlined by Scase et al. (2006).

In particular, Caulfield and Woods (1995) predicted for forced, pure or disturbed plumes with $\sigma \ll 1$ that the maximum rise height should be scaled as

$$Z_{\mathrm{m}} \propto F_0^{1/4} N^{-3/4} = \sigma^{-3/8} H_{\mathrm{p}}, \tag{2.17}$$

consistent with (2.14). Although those studies focused upon the maximum rise height, Z_{m}, and not the spread height, Z_{s}. By determining the relationship between Z_{m} and Z_{s} for experiments with wide ranging σ, we are able to draw a connection between that body of work and our study of intrusions.

2.3 Intrusion spread in the buoyancy-inertia regime

As well as determining the spread height, we wish to determine the structure and evolution of the radially spreading intrusion. Most studies of radially

spreading intrusions ignore the dynamics of the plume and assume a source of uniform density fluid already at its neutral buoyancy level.

A plume in a uniformly stratified ambient overshoots its neutral buoyancy level to a maximum height then collapses to spread radially outwards as an intrusive gravity current at its neutral buoyancy level. The radial spread of the intrusion front position in time is predicted to follow a power law relationship in the form $R_{\mathrm{f}}(t) \sim t^P$, where "p" is dependent upon the spreading regime of the flow.

In Sections 2.3.1-2.3.3, we derive the theory to analyze the intrusion radial spread in time at its neutral buoyancy level. We consider the rate of intrusion spread only in the buoyancy-inertia regime of a uniformly stratified ambient. For large volcanic eruptions spreading in the stratosphere, the intrusion front is first observed by satellite at a radius close to the start of the model-predicted buoyancy-inertia regime (Baines and Sparks, 2005). Spreading in the stratosphere is observed to be unaffected by stratospheric winds and Coriolis force during the first few hours of the spread (Baines and Sparks, 2005). Hence, our study could be connected to the spreading umbrella cloud at early times after the initial explosion.

There are two models to be considered. Each model uses one of two assumptions about the source conditions at the start of the buoyancy-inertia regime, where the radius, $r=R_1$. The first model considers a constant radial volume flux and the other considers a constant buoyancy flux to the radial spreading intrusion at its neutral buoyancy level. In another assumption where the supply of volume or buoyancy flux is constant but the structure is assumed to be self-similar, the radial advance is shown to transition follows a between two power law relationships.

2.3.1 Spreading rate assuming constant volume flux

A straightforward application of self-similarity theory takes a box-model approach (Huppert and Simpson, 1980). The speed, u_f, of the intrusion front with constant height, h_f, in a uniformly stratified fluid is given by

$$u_f = \text{Fr } Nh_f, \tag{2.18}$$

in which the Froude number, Fr, is assumed to be constant. Shallow water theory and lock-release experiments of intrusions in uniformly stratified ambient fluid predict that $\text{Fr} \simeq 1/4$ (Ungarish, 2006; Sutherland et al., 2007; Bolster et al., 2008). In its application to the intrusion spreading from the large volcanic eruptions of Mount Pinatubo (Holasek et al., 1996b), Fr was observed to be approximately 0.3 not too different from this prediction of 1/4. The velocity of the intruding fluid is also given by

$$u_f = dR_f/dt. \tag{2.19}$$

To close the problem, we can make one of two assumptions about the source conditions at R_1. In one approach, we assume no entrainment into the intrusion so that the volume of the intrusion should increase in time as

$$Q_i = 2\pi(R_f - R_1)h_f u_f \tag{2.20}$$

in which $Q_i \simeq Q_1 \ (\simeq 2\pi R_1 h_1 u_1)$ is the volume flux of the source emanating from a radius, R_1 with speed, u_1 and thickness, h_1.

Using this in (2.18) to eliminate h_f, the resulting equation for the advance of the intrusion front becomes (Chen, 1980; Lemckert and Imberger, 1993;

Devenish and Rooney, 2014)

$$\frac{dR_f}{dt} = u_f = \left(\frac{\text{Fr}\, NQ_i}{2\pi}\right)^{1/2} (R_f - R_1)^{-1/2}.$$

Solving with the assumption that the front first forms at time, t_1 gives the front position, $R_{fQ}(t)$, for constant volume flux forcing:

$$R_{fQ} - R_1 \simeq \left(\frac{3}{2}\right)^{2/3} \left(\frac{\text{Fr}}{2\pi}\frac{Q_i}{N}\right)^{1/3} [N(t - t_1)]^{2/3}. \tag{2.21}$$

The characteristic reduced gravity, g_i', between a well-mixed intrusion and the surrounding ambient over the thickness, h_1, of the intrusion at R_1 is (Sparks et al., 1997; Ungarish, 2006)

$$g_i' \approx N^2 h_1 \tag{2.22}$$

This expression (2.21) can be written in terms of the buoyancy flux, F_i, at R_1 through the relation

$$F_i \equiv Q_i g_i' \sim Q_i N^2 h_1. \tag{2.23}$$

In the box-model, $h_1 = h_f$, the depth of the intrusion over its length from R_1 to R_f. Hence, (2.21) becomes

$$R_{fQ} \simeq \left(\frac{3}{2}\right)^{2/3} \left(\frac{\text{Fr}}{2\pi h_1}\frac{F_i}{N^3}\right)^{1/3} [N(t - t_1)]^{2/3}. \tag{2.24}$$

Substituting (2.21) back into (2.20) gives the intrusion height, which for $t \gg t_1$ and $R_f \gg R_1$ satisfies

$$h_{fQ} \propto t^{-1/3} \propto R_f^{-1/2}. \tag{2.25}$$

2.3.2 Spreading rate assuming constant buoyancy flux

In a separate approach[1], we suppose a constant buoyancy flux, F_i, from the source. We do not need to neglect the effects of entrainment in this case. While fluid entrained into the current head decreases its relative buoyancy, it also increases in height. Assuming the density of the entrained ambient fluid is approximately constant, the two effects conspire to maintain a constant buoyancy, if not volume flux. Using (2.20) and (2.23), the buoyancy flux at the source is

$$F_i \sim 2\pi N^2 (R_{\mathrm{f}} - R_1) h_f{}^2 u_{\mathrm{f}}, \tag{2.26}$$

As above, we use this expression to eliminate h_f in (2.18) to get

$$\frac{dR_{\mathrm{f}}}{dt} = \left(\frac{\mathrm{Fr}^2 F_i}{2\pi}\right)^{1/3} (R_{\mathrm{f}} - R_1)^{-1/3}.$$

From this it follows that the front position, R_{f}, for constant buoyancy flux forcing is given by

$$R_{\mathrm{f}} - R_1 \simeq \left(\frac{4}{3}\right)^{3/4} \left(\frac{\mathrm{Fr}^2}{2\pi} \frac{F_i}{N^3}\right)^{1/4} [N(t - t_1)]^{3/4}. \tag{2.27}$$

This power law dependence, in the limit $t \gg t_1$ and $R_{\mathrm{f}} \gg R_1$, was also found (Didden and Maxworthy, 1982; Kotsovinos, 2000) by assuming constant volume flux and balancing inertia and buoyancy forces written in terms of g', not N.

From (2.27) and assuming $t \gg t_1$ and $R_{\mathrm{f}} \gg R_1$, it follows that the intrusion height changes with time and front-radius as

$$h_{fF} \propto t^{-1/4} \propto R_{\mathrm{f}}^{-1/3}. \tag{2.28}$$

---

[1]Paul F. Linden,private communication,2013
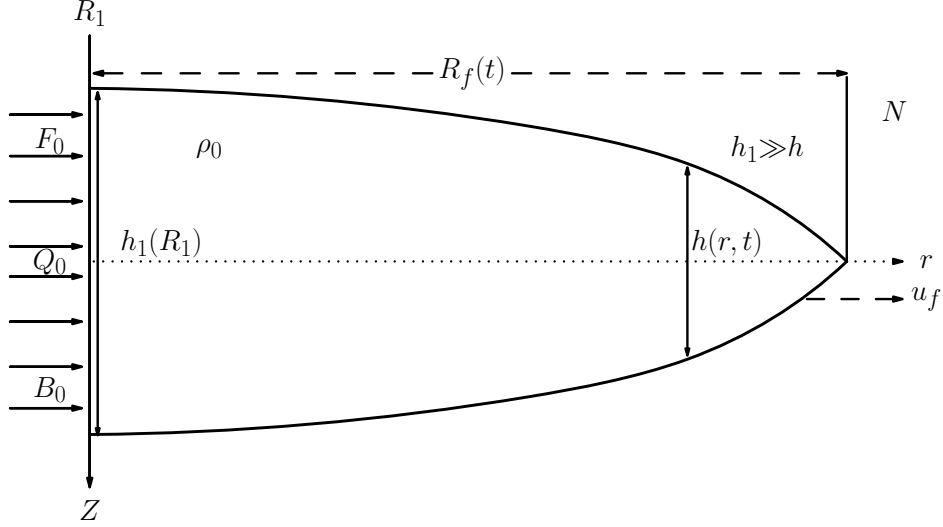
Figure 2.4: Side-view of a forced plume spreading at its neutral buoyancy level in uniformly stratified ambient. The radius incident at the spreading depth is denoted by R_0, the radius at the start of the buoyancy-inertia regime is given by R_1 and the position of the intrusion radial front position in time is given by R_f.

In both (2.25) and (2.28), the intrusion height (constant along its length) decreases in time. However, one does not expect the intrusion height at its source to be influenced by its downstream evolution.

2.3.3 Spreading rate for constant volume or buoyancy flux

Assuming the source conditions are fixed and the height, h_1, is constant at R_1, we consider how the shape of the intrusion head influences the supplied volume and buoyancy fluxes.

We suppose the depth, $h(r, t)$, of the intrusion along its radius adopts a self-similar shape of the form

$$h = h_1 \left(\frac{R_f - r}{R_f - R_1} \right)^{P_h}, \tag{2.29}$$

in which $R_{\mathrm{f}} = R_{\mathrm{f}}(t)$ and P_h is some constant exponent. Figure 2.4 shows a schematic of the intrusion thickness with the above labelled parameters. The volume of the intrusion is

$$V = 2\pi \int_{R_1}^{R_{\mathrm{f}}} h \; r \; dr$$

$$= \frac{2\pi h_1}{(P_h + 1)(P_h + 2)} \left[(R_{\mathrm{f}} - R_1)^2 + (R_{\mathrm{f}} - R_1)R_1(P_h + 2) \right],$$

(2.30)

which is simplified to give

$$V = \frac{2\pi h_1}{(P_h + 1)(P_h + 2)} [R_{\mathrm{f}}^2 - R_1^2 + P_h R_{\mathrm{f}} R_1 - P_h R_1^2]. \qquad (2.31)$$

The buoyancy associated with the intrusion is

$$B = 2\pi N^2 \int_{R_1}^{R_{\mathrm{f}}} h^2 \; r \; dr$$

$$= \frac{\pi h_1{}^2 N^2}{(2P_h + 1)(2P_h + 2)} \left[(R_{\mathrm{f}} - R_1)^2 + (R_{\mathrm{f}} - R_1)R_1(2P_h + 2) \right],$$

(2.32)

which is simplified to give

$$B = \frac{\pi h_1{}^2 N^2}{(2P_h + 1)(2P_h + 2)} [R_{\mathrm{f}}^2 - R_1^2 + 2R_{\mathrm{f}} R_1 P_h - 2P_h R_1^2]. \qquad (2.33)$$

The formulae predict that the intrusion volume and buoyancy increase as $R_{\mathrm{f}} - R_1$ increases in time as

$$Q_0 = \frac{dV}{dt} \qquad (2.34)$$

and

$$F_0 = \frac{dB}{dt} \qquad (2.35)$$

respectively. If the volume or buoyancy flux at R_1 is constant, then one

expects

$$R_\mathrm{f} - R_1 \propto \begin{cases} t - t_1 & t \gtrsim t_1 \\ t^{1/2} & t \gg t_1 \end{cases}, \tag{2.36}$$

independent of the value of P_h. The transition from early to late occurs when the front is situated at

$$R_\mathrm{fc} \simeq R_1(3 + CP_h), \tag{2.37}$$

with $C{=}1$ assuming volume is conserved and $C{=}2$, assuming buoyancy is conserved. This implies that the intrusion front position should first increase linearly in time and then increase as the square-root of time.

These three different theoretical predictions for the intrusion front position and its structure as a function of time are used to model the plume spreading at its neutral buoyancy level. Experiments will be use to test the validity and consistency of these predictions in (2.24), (2.27) and (2.36) above.

2.4 Intrusion Spread in the viscous-inertia regime

A forced plume collapses and spreads radially as an intrusive gravity current at its neutral buoyancy level in a uniformly stratified ambient. Beyond the buoyancy-inertia regime its velocity decreases as turbulent stresses overtake the spreading intrusion front. While viscous effects become dominant over the buoyancy effects acting on the flow, the intrusion front reaches the start of the viscous-inertia regime, R_v, and extends into this regime.

Although this is not the focus of our research, we review predictions for the intrusion radial advance in time, $R_\mathrm{v}(t)$, in the viscous-inertia regime. This obeys the power law (Lemckert and Imberger, 1993):

$$R_\mathrm{v} \sim \left(\frac{Q_0^4 N^2}{\nu} \right)^{1/10} t^{1/2} \tag{2.38}$$

with a proportional constant of 0.45 (Chen, 1980). From the continuity equation the intrusion volume changes in time, position and thickness as(Huppert, 1982)

$$Q_0 t \sim h(t) R_\mathrm{f}^2. \tag{2.39}$$

From (2.39), it follows that the intrusion thickness in the viscous-inertia regime is given by

$$h_\mathrm{v} \sim \left(\frac{Q_0 \nu}{N^2}\right)^{1/5} \tag{2.40}$$

which is independent of its position and time. The proportionality constant for this relationship was found through experiments to be 0.51 (Chen, 1980; Zatsepin and Shapiro, 1982) and 1.7 (Kotsovinos, 2000). Similarly from (2.21) for $R_\mathrm{f} \gg R_1$, the intrusion thickness is given by

$$h_\mathrm{I} \sim \left(\frac{Q_0}{N R_\mathrm{f}}\right)^{1/2} \tag{2.41}$$

which implies that h_I increases as $R_\mathrm{f}^{-1/2}$ from its front position to the plume centreline at the spreading depth, Z_s.

Balancing (2.40) and (2.41) give (Lemckert and Imberger, 1993; Devenish and Rooney, 2014)

$$R_v = C_v \left(\frac{Q_0^3}{N \nu^2}\right)^{1/5}, \tag{2.42}$$

for the radius of the intrusion at the start of the viscous-inertia regime where C_v is the constant of proportionality.

Chapter 3

Experiments: Measurement Methods & Qualitative Results

3.1 Introduction

This chapter presents the experimental work done on investigating the spread of a radial intrusion created from a forced turbulent plume in a uniformly stratified fluid. As the plume first hits its neutral buoyancy level, it overshoots this level behaving like a negatively buoyant fountain. It then stops at its maximum penetration depth as its mean momentum flux, hence, its vertical velocity, goes to zero. The fluid then collapses and ultimately spreads radially at its neutral buoyancy level. In this chapter we seek to extend our understanding of the dynamics of turbulent plumes in uniform stratification through measurements of the maximum depth, Z_{m}, the spreading depth, Z_{s}, and the rate of spread of the radial intrusion front in the buoyancy-inertia regime. Further analysis on the intrusion thickness as a function of radius and time, $h(r,t)$ will also be discussed. Besides a detailed explanation on the experimental design and setup is outlined in the following section.

One of the earliest studies was performed by Morton et al. (1956), who conducted a series of laboratory experiments to derive the equations of the momentum, mass and energy fluxes that predicted the evolution of a buoyant plume. They also theoretically showed the dependence of the source momentum, volume and buoyancy fluxes on the plume maximum rise height in a uniformly stratified fluid as stratification becomes important.

Turner (1966) showed the interaction of the upward and downward flows of the plume such that it reduces the maximum height, Z_{m}, to a smaller value after some time, t. Using dimensional arguments Z_{s} was used to develop a relationship between the momentum and buoyancy fluxes at the source.

Maxworthy (1972) also performed one of the earliest studies to investigate the spread of an intrusion emanating from a jet in a stratified ambient fluid. He theoretically derived the equations to predict the radial spread of an intrusion as a function of time (see Table 3.2) then conducted a series of experiments for comparison.

Experimental studies were also conducted on fountains in uniformly stratified ambient fluid by Bloomfield and Kerr (1998). They investigated the initial height also referred to as the maximum penetration height, the final height also called the steady state height and spread height of a fountain by showing their dependence upon the source momentum, volume and buoyancy fluxes when stratification is critical. This extended the work done by Turner (1966).

One major concern was to determine the power law relationship in the form $R_{\mathrm{f}} \sim t^{\mathrm{P}}$ that correctly predicts the intrusion radial spread in time in the buoyancy-inertia regime created as the plume collapses and spreads. The power, P, has varied for different studies as shown in Table 3.2 below. Kotsovinos (2000) resolved this issue through a series of experiments used to charac-

terize the radial spread of the intrusion into four distinct regimes: the radial jet regime, the radial momentum flux regime, the buoyancy-inertia regime and the viscous-inertia regime. These regimes were distinguished based upon the magnitude of the forces that act on the intrusion as it propagates and using different scaling analysis.

In Section 3.2 we explicitly discuss the laboratory experimental set-up and analysis of the current research. This section outlines the experimental design and techniques used to qualitatively analysis the experiments. In Section 3.2.4 we also discuss the qualitative and quantitative observations and analysis from the experiments.

3.2   Experimental Setup & Analysis Methods

3.2.1   Experimental Setup

Laboratory experiments were conducted to gain insight into the spreading of an intrusion at its neutral buoyancy level resulting from an axisymmetric buoyant plume in a uniformly stratified ambient. Experiments were conducted in one of two acrylic tanks: a cubical tank measuring 39.50 cm on each side and a wider tank measuring 120.00 cm long by 120.00 cm wide by 29.50 cm high. In the cubical tank the radial spreading intrusion created spread over a short distance but in the wider tank the plume spread over large vertical distances up to 40 cm from the plume centreline at the neutral buoyancy level. Hence, for all experiments the intrusion spread within the buoyancy-inertia regime was observed.

In both cases, the plume was injected downward into the centre of the tank, and the ambient stratification and source flow rate were established to ensure the plume did not impact the bottom of the tank. After reaching its

maximum depth, Z_{m}, it falls back to Z_s and intrudes radially outward at its neutral buoyancy level.
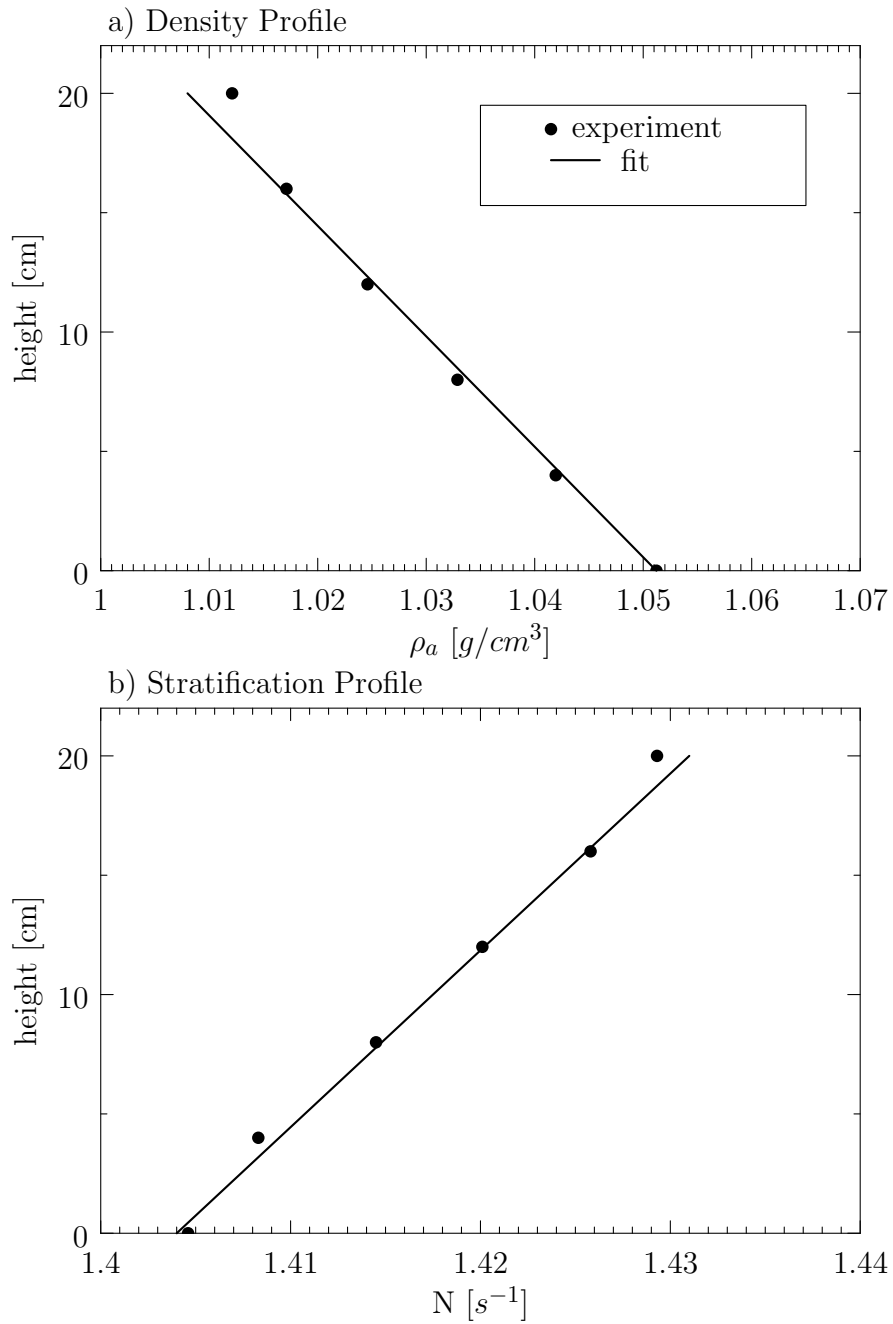
Figure 3.1: Profiles of a) density with corresponding b) stratification of $N \simeq$ 1.42 s^{-1} for an experiment conducted in the wide tank.

3.2.2 Density Measurements

A uniformly stratified ambient fluid was created using the double bucket technique (Oster, 1965). The total ambient depth was $H_T \simeq 30$ cm and 20 cm in the cubical and wide tanks respectively. The density profile of the ambient fluid created in the tank was recorded by taking samples at 5 cm intervals and measured their densities with an Anton Paar DMA 4500 Densitometer that measured the salt content of the fluid. In some experiments a traversing conductivity probe (Precision Measurement Engineering MSCTI) mounted onto a vertical traverse was also used to measure the density profile of the ambient and the density profile across the spreading intrusion at a fixed radius far from the plume centerline. The measured background density at corresponding heights confirmed a linear density profile for all experiments. An example is shown in Figure 3.1(a) with its corresponding stratification profile (b). The buoyancy frequency, N, characterized the uniform stratification with N ranging from $0.70s^{-1}$ to $1.50s^{-1}$ in all our experiments.

The density of the plume at the source was established through the addition of salt to $3-4$ L of water in a uniformly mixed reservoir. In most experiments, the reservoir fluid was then dyed with red or blue food coloring. The dye used did not change the density of the plume fluid but served to improve the contrast of images recorded from the experiment by the digital video camera. The resulting density of the source fluid, ρ_0, ranged from 1.01 ± 10^{-5} g/cm^3 to 1.14 ± 10^{-5} g/cm^3, as measured by the Anton Paar DMA 4500 Densitometer.

3.2.3 Other Measured Source Conditions

The fluid was injected vertically downwards into the tank through one of two nozzles with the opening 0.50 cm below the surface of the ambient fluid. The
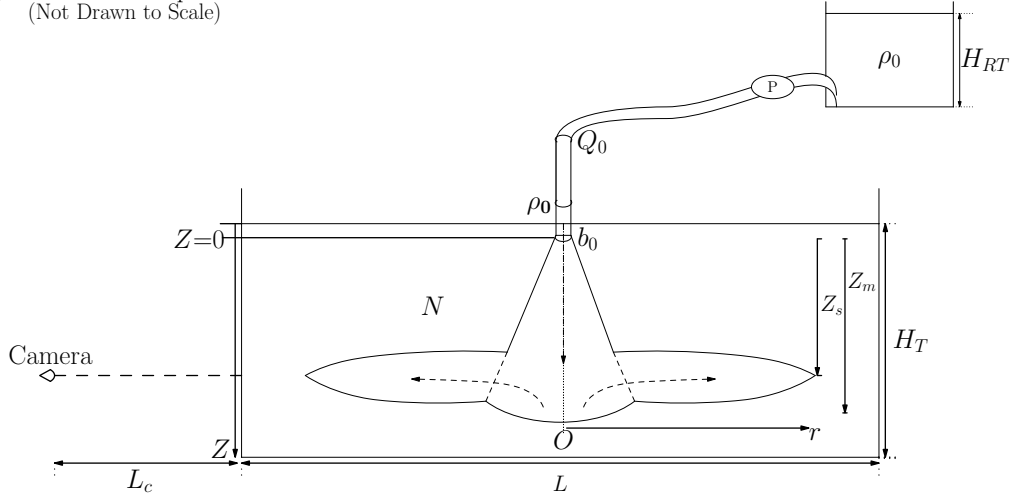
Figure 3.2: Experimental set-up and definition of parameters .

small nozzle of radius b_0=0.10 cm, was fitted with a 0.05 cm mesh attached horizontally across the opening. The larger nozzle, of radius, b_0=0.28 cm, was fitted with six cross-wires spanning its opening. The mesh and cross-wires ensured that the flow leaving the nozzle was turbulent. For all our experiments, the Reynolds number of such flows at the nozzle depth ranged from Re_0=387 to Re_0=1878. Such high Reynolds number flow have vertical motion that exceeds the effects of viscosity as the fluid falls to a relatively large vertical distance in the ambient fluid as shown in our experiments. Figure 3.3 shows an example of a typical experiment conducted in the wide tank.

Faster flow rates were achieved with the larger nozzle as the smaller nozzle only produced flow rate, $Q_0 \lesssim 6$ cm^3/s. The Froude number ranged from Fr_0=5 to Fr_0=156 for all our experiments.

Most experiments injected fluid from the reservoir through a centrifugal salt-water pump (HYDOR 200) with unimpeded flow rate. The actual flow rate through the nozzle was controlled by adjusting a clamp. The flow rate was measured by a flow meter (Muis Controls Ltd., P24/1-044-40C), and the

Figure 3.3: Side-view snapshot of an experiment performed in the wide tank with N=1.40 s^{-1}, ρ_0=1.020 g/cm^3, Q_0=7.4 cm^3/s and b_0=0.28 cm at times, t=90 s.

desired flow rate through the nozzle was controlled by adjustment of the flow meter within the first $3-5$ s of an experiment. In our experiments, the flow rate, Q_o, through the nozzle opening ranged from 3 cm^3/s to 12 cm^3/s.

Beside and behind the acrylic tank walls fluorescent light sources were positioned to illuminate the tank interior. White plastic sheets were placed onto the outer walls of the tank to diffuse the incoming fluorescent light. A side-view of the flow evolution was recorded by a digital video camera (Panasonic HDC HS250) that was positioned at $L_c\sim3$ m from the front wall of the tank with the lens approximately at the vertical level of the radially spreading intrusion. A still digital camera also recorded snapshots of the flow and intrusion cross-section seen through the top of the tank, as shown in Figure 3.6. Each experiment lasted between 80 s to 290 s.

At the end of each experiment a square grid was positioned horizontally and vertically inside the tank so that the camera could record known lengths for the subsequent digital processing.

The three important parameters that were controlled in each experiment giving the source conditions of the plume are the flow rate, Q_0, the ambient density, $\bar{\rho}(z)$, and the source fluid density, ρ_0, inside the reservoir as shown in Figure 3.2. The measured results from our experiments are shown in Table

42

3.1. From these we found the source momentum flux, M_0 (2.1), buoyancy flux, F_0, (2.2) and buoyancy frequency, N, (2.10) for each corresponding experiment as shown in Table 3.1. A total of 22 experiments were performed in both cubical and wide tanks used with one of the three parameters (Q_0, $\bar{\rho}(z)$ or ρ_0) varied at a time.

3.2.4   Analysis Methods and Qualitative Results

In this section we present the analysis methods used to examine qualitatively the laboratory experiments recorded by the digital video camera. Figures 3.5 and 3.6 show snapshots taken at different times and perspectives of a typical experiment. As the plume initially moved downward away from the source, it expanded due to turbulent entrainment (Figure 3.5a). As it moved further away, it became negatively buoyant due to turbulent mixing, reached a maximum depth and collapsed back upon itself. This collapsing fluid reached its neutral buoyancy level (found at Z_s where the buoyancy flux vanishes) and then began to spread radially outwards (Figure 3.5b). The front of the radially spreading intrusion advanced in time over the duration of the experiment (Figure 3.5c). A top view of this experiment (Figure 3.6) showed that the spreading was not axisymmetric as azimuthal instabilities developed along the boundary of the intrusion front. These disturbances grow into well defined eddies that became more evident as the intrusion front position increases in time. Azimuthal instabilities occur as a consequence of the interaction between the radial spreading intrusion head height and the stratified interface ahead of the intrusion front. As the vertical extent of the intrusion head decreases with radial distance traveled it becomes comparable with the stratified interface. Such lobate structures were also observed to develop in the umbrella cloud emanating from the June 15, 1991, Mount Pinatubo erup-

Table 3.1: Summary of the measured and computed data for all our experiments where expt is the experiment number, $\bar{\rho}(0)$ [g/cm^3] is the ambient density at the surface or nozzle depth, $\bar{\rho}(H)$ [g/cm^3] is the ambient density at the bottom of the tank, ρ_0 [g/cm^3] is the source fluid, b_0 [cm] is the radius of either of the two nozzles used, Q_0 [cm^3/s] is the flow rate, M_0 [cm^4/s^2] the momentum flux, F_0 [cm^4/s^3] the buoyancy flux, N [s^{-1}] the ambient stratification, H_{p} [cm] the jet length and σ the dimensionless parameter.

| | | Measured parameters | | | | Calculated parameters | | | | |
| | | | | | | Source Conditions | | | Plume Scales | |
Expt	$\bar{\rho}(0)$	$\bar{\rho}(H)$	ρ_0	b_0	Q_0	M_0	F_0	N	H_{p}	σ
1	1.01	1.05	1.10	0.1	3.4	256	278	1.08	3.83	0.99
2	1.01	1.05	1.14	0.1	3.7	303	477	1.12	3.32	0.51
3	1.01	1.05	1.14	0.1	4.6	468	559	1.14	4.25	0.91
4	1.01	1.05	1.14	0.1	3.7	303	469	1.11	3.35	0.51
5	1.01	1.05	1.14	0.1	3.7	303	469	1.13	3.35	0.53
6	1.01	1.05	1.14	0.1	3.7	303	461	1.11	3.38	0.53
7	1.01	1.05	1.10	0.1	5.9	770	482	1.12	6.66	3.20
8	1.01	1.05	1.07	0.28	7.6	243	408	1.4	3.05	0.69
9	1.01	1.05	1.07	0.28	11.6	566	641	1.5	4.59	1.76
10	1.01	1.05	1.07	0.28	9.20	356	517	1.41	3.61	0.94
11	1.02	1.05	1.07	0.28	9.20	356	459	1.38	3.83	1.15
12	1.02	1.04	1.07	0.28	7.20	218	343	1.34	3.07	0.73
13	1.01	1.05	1.07	0.28	9.80	404	517	1.47	3.97	1.32
14	1.01	1.05	1.07	0.28	8.80	326	10.3	1.44	24.0	2097
15	1.01	1.05	1.14	0.28	8.50	304	1054	1.4	2.24	0.16
16	1.01	1.05	1.03	0.28	8.40	297	158	1.42	5.69	7.12
17	1.01	1.05	1.02	0.28	7.40	231	40	1.4	9.34	64.8
18	1.01	1.03	1.02	0.28	7.40	231	42.4	1.17	9.08	40.4
19	1.00	1.01	1.01	0.28	8.20	283	51.4	0.75	9.63	17.1
20	1.01	1.02	1.01	0.28	8.00	269	38.2	0.89	10.8	39.4
21	1.00	1.01	1.01	0.28	3.40	49	16.3	0.75	4.56	5.01
22	1.01	1.03	1.01	0.1	3.20	43	13.7	0.84	4.54	6.97
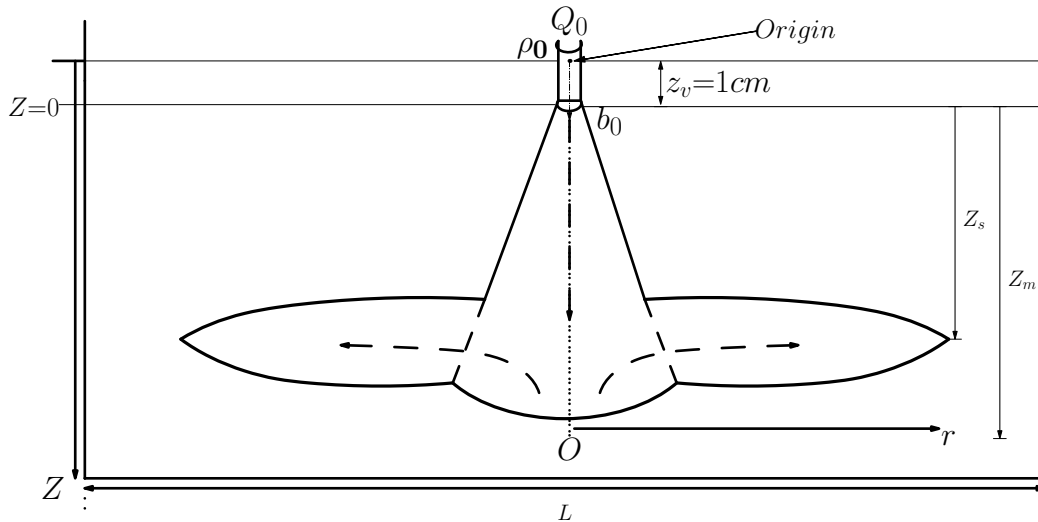
Figure 3.4: shows the virtual spread height, Z_{sv}, and virtual maximum height, Z_{mv} with virtual origin for all our experiments

tion (Holasek et al., 1996b). The analysis of these instabilities lies beyond the scope of this research. However, we found that analysis of the intrusion at its neutral buoyancy level on either side of the central plume as recorded by the side-view camera was sufficient to characterize the mean speed and shape of the intrusion when compared with the corresponding top view of the experiment.

From snapshots taken at times after the intrusion was fully-developed (Figure 3.5c), we measured the intrusion spreading depth, Z_s=5.0 ($\pm$0.2) cm, and maximum plume depth, Z_m=9.0 ($\pm$0.1) cm for the same experiment shown in Figure 3.5. Assuming a linear spread with height of the forced plume near the source with spreading rate (Lee and Chu, 2003) 0.23, its virtual origin is situated $z_v \simeq 1$ cm above the nozzle opening position at Z=0. Thus, we define the distance from the virtual origin to the intrusion and maximum plume depth to be Z_{sv}=6.0 cm and Z_{mv}=10.0 cm, respectively. Figure 3.4 shows the virtual spreading height, Z_{sv}, and virtual maximum height, Z_{mv}, in our experiments.
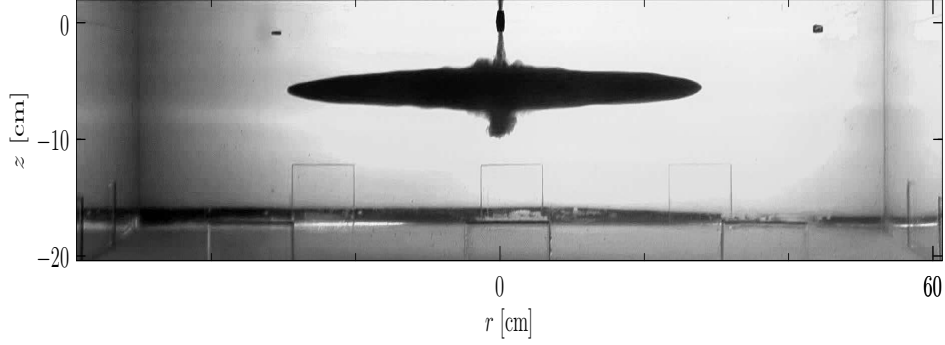
a) t = 1s (side view)

b) t = 20s (side view)
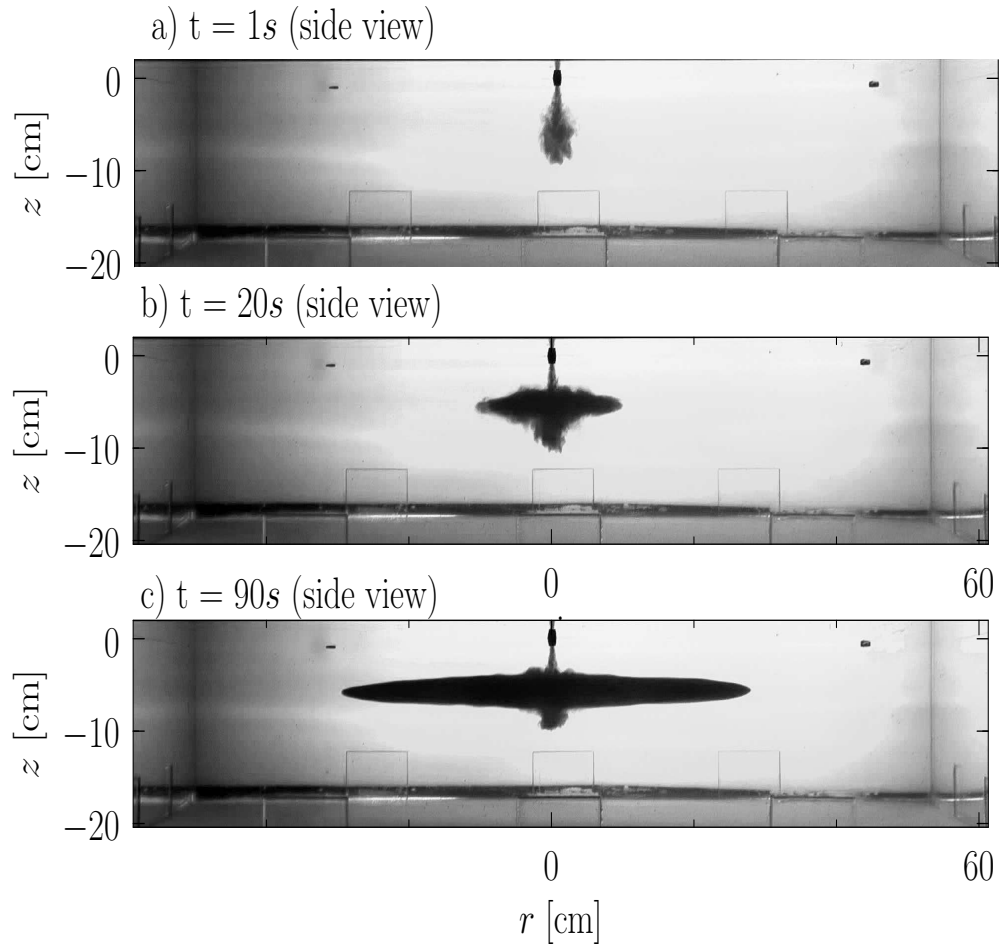
c) t = 90s (side view)

Figure 3.5:   Snapshots of an experiment performed in the wide tank with N=1.40 s^{-1}, ρ_0=1.020 g/cm^3, Q_0=7.4 cm^3/s and b_0=0.28 cm showing side-views at times a) t=1 s, b) t=20 s and c) t=90 s.
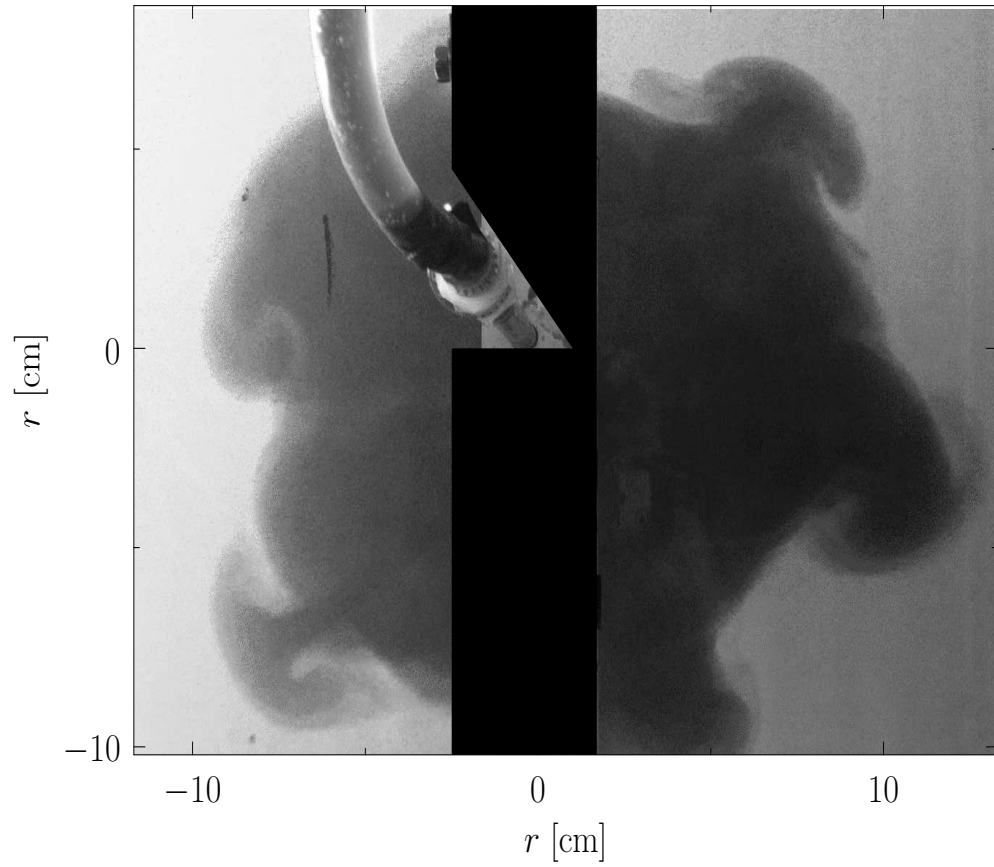
Figure 3.6:   Snapshot of the same experiment shown in Figure 3.5 with N=1.40 s^{-1}, ρ_0=1.020 g/cm^3, Q_0=7.4 cm^3/s and b_0=0.28 cm from top view at $t \simeq 60$ s.

3.2.5 Intrusion Spreading Regimes

In general, the intrusion created from a forced turbulent plume in a uniformly stratified ambient exhibits four distinct regimes (Chen, 1980; Zatsepin and Shapiro, 1982; Kotsovinos, 2000; Lister and Kerr, 1989). Kotsovinos (2000) characterized these regimes as the radial jet regime, the radial momentum flux regime, the buoyancy-inertia regime and the viscous-inertia regime. These regimes were distinguished based upon different scaling analysis and the magnitude of the forces acting upon the intrusion as it propagates at its neutral buoyancy level (Kotsovinos, 2000). In each regime, the radial spread as a function of time was experimentally determined with evidence of factors that may or may not contribute to its radial spread.

These flow regimes were observed in our experiments as the plume collapses and spreads radially outwards forming an intrusive gravity current. However, the focus was upon the intrusion spread in the buoyancy-inertia regime. The application of our results to real volcanic eruptions spreading in the stratosphere is particularly useful when the intrusion speed exceeds stratospheric wind speed, and as the intrusion becomes unaffected by such winds for spreading in this regime (Baines and Sparks, 2005). Thus the intrusion front is assumed to spread symmetrically in the buoyancy-inertia regime (Baines and Sparks, 2005).

We also found the radius, R_0 incident at the spreading depth, Z_s, and the radius at the start of the buoyancy-inertia regime, R_1. The radial position, R_1, was difficult to define. Figure 3.7 illustrates these positions of the intrusion spread in a uniformly stratified ambient fluid.
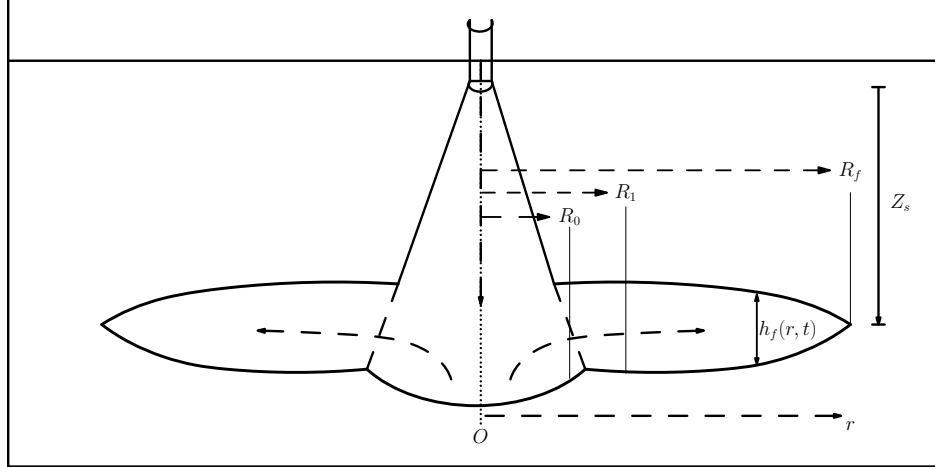
Figure 3.7: Side-view of a forced plume spreading at its neutral buoyancy level in uniformly stratified ambient. The radius incident at the spreading depth is denoted by R_0, the radius at the start of the buoyancy-inertia regime is given by R_1 and the position of the intrusion radial front position in time is given by R_f all measured from the plume origin, O.

3.2.6 Radial distance (R_f) as a function of time (t)

This section describes the analysis technique used to obtain the intrusion radial spread as function of time, $R_f(t)$. The top-view snapshots of the intrusion spread were not always axisymmetric (see Figure 3.6), even though the corresponding side-view snapshots of the intrusion spread seem symmetric as shown in Figure 3.5. Nonetheless, from side-view snapshots of the intrusion spread we were able to show the radial intrusion front position in time.

To measure the formation and radial spread of the intrusion over time, we constructed horizontal time series taken at the spreading depth, Z_s, as shown in Figure 3.8. At early times shortly after the forced plume first passed the level Z_s, we identified the central plume radius, R_0. In this experiment, $R_0 = 1.0(\pm 0.3)\,\text{cm}$.

At later times the effects of azimuthal instabilities along the intrusion front (e.g. see Figure 3.6) were evident in the horizontal time series as thin regions of lower intensity light. The intensity variation was caused by the

azimuthal instabilities along the intrusion front position. These intensity variations and the difference between left- and right-propagating fronts were used to estimate the error of the intrusion front position, $R_f(t)$.
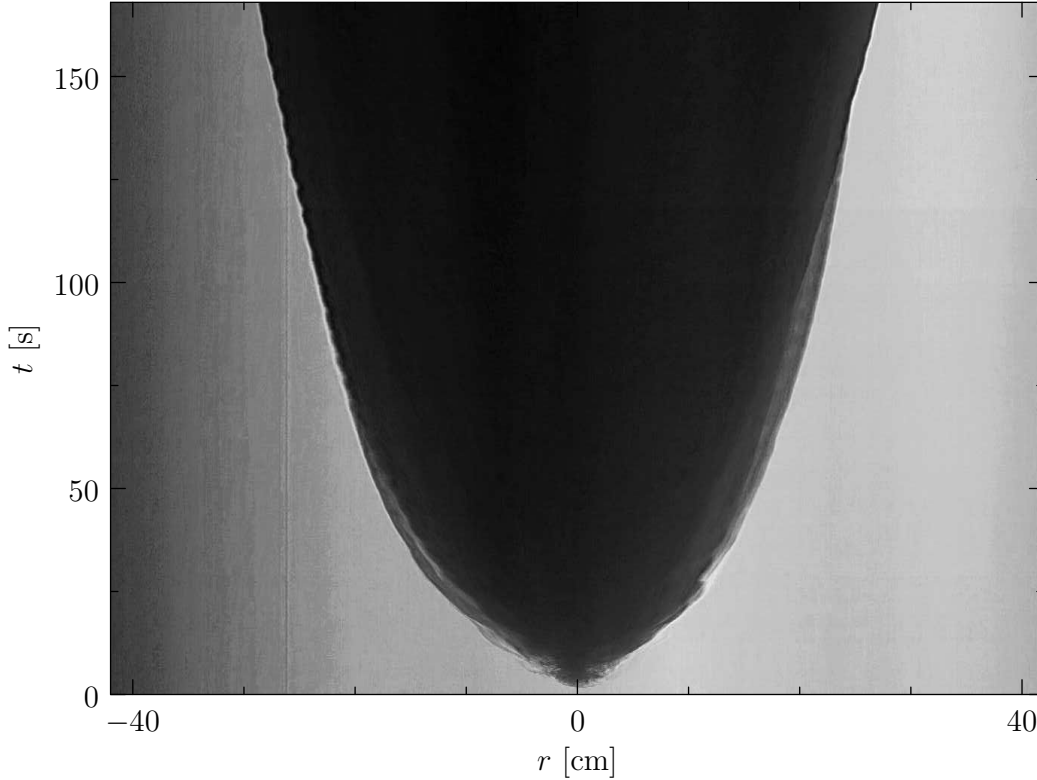
Figure 3.8: Horizontal time series constructed from the experiment shown in Figure 3.5 with the time evolution being examined along a horizontal slice taken at the spreading level of the intrusion, $z = Z_s = 5\,\mathrm{cm}$.

To aid in the determination of $R_f(t)$, the intensity contrast between the intrusion and ambient was enhanced. Using the image analysis software provided by Matlab, an averaging filter was used to smooth along the intrusion front. By replacing each radial point, R_f, represented by a pixel with the average of neighbouring pixel points at time, t, along the intrusion radial spreading front position we obtained $R_f(t)$. This increased the contrast of the image. Contours were then matched to the enhanced image of the intrusion front position and these points were extracted to form $R_f(t)$. The result is shown in Figure 3.9a. This shows the intrusion front advanced radially

outward though at a slower speed at later times ($t > 15$ s).

The advance of the front exhibited two distinct regimes of behaviour as evident through the log-log plot shown in Figure 3.9b. These regimes are the buoyancy-inertia regime and the viscous-inertia regime. The viscous-inertia regime is first seen where the data points deviate from the slope as shown in Figure 3.9b. As the intrusion front advances in time its head height decreases and azimuthal instabilities grow, as a result viscosity becomes dominate and the speed of the front decreases to satisfy the requirement of mass conservation. Here R_1 and t_1 are the radius and corresponding time, respectively, when the intrusion front first began to spread radially outward in the inertia-buoyancy regime.

To determine R_1, we assumed that $\Delta R_f \equiv R_f - R_1$ versus $\Delta t \equiv t - t_1$ should follow a power law relationship for $R_f \gtrsim R_1$. Thus, we constructed a sequence of $\log(R_f - R')$ versus $\log(t - t')$ plots, in which R' ranged from R_0 to $5R_0$ and t' was defined implicitly by $R' = R_f(t')$. To each plot the corresponding best-fit line and corresponding correlation coefficient were computed. R_1 was chosen to be the minimum value of R' for which the correlation coefficient, C_r^2, was largest, typically $C_r^2 \gtrsim 98\%$. That is, R_1 and t_1 are the smallest values beyond which power-law behaviour was well-established. For the data shown in Figure 3.9, we found $R_1 \simeq 3.1\ (\pm 0.2)\,\mathrm{cm}$ and $t_1 \simeq 5.0\ (\pm 0.1)\,\mathrm{s}$.

In this, as in most experiments, we found that the front position obeys a power law over tens of seconds. Explicitly, for the data in Figure 3.9, we found $R_f - R_1 \simeq 0.94\ (\pm 0.01)\ (t - t_1)^{0.780\ (\pm 0.004)}$. The error in the exponent was determined from the error of the best-fit line. However, azimuthal instability and differences in the power computed from the leftward and rightward propagating fronts observed from the side-view of the intrusion resulted in a larger error on the order of ± 0.15 on the exponent.

a) Front Position vs Time

b) Log-log Plot

Slope: 0.78 ± 0.02
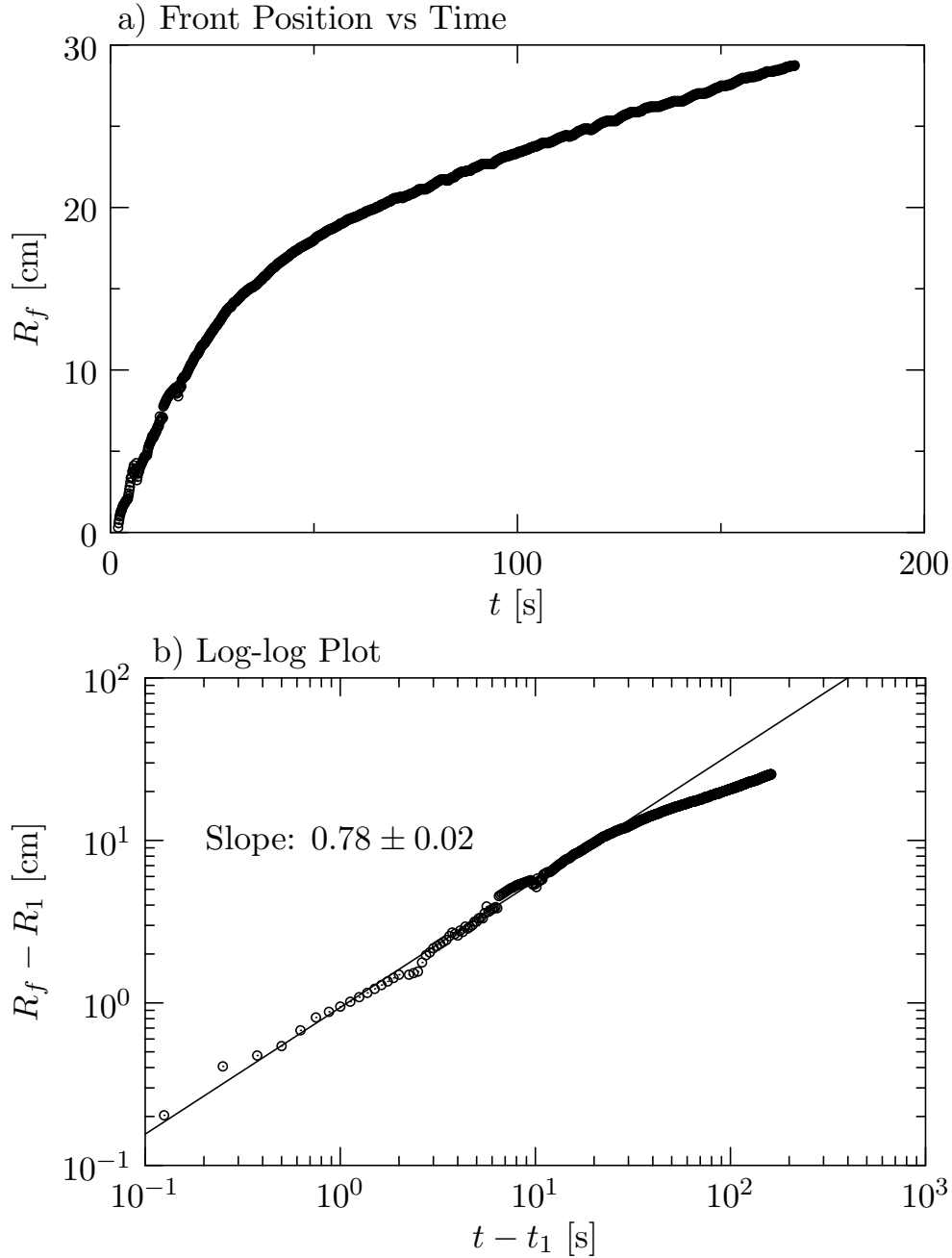
Figure 3.9: From the horizontal time series shown in Figure 3.8, plots of a) the radial distance, R_f, of the intrusion front from the plume centerline as a function of time, t, with $t = 0$ corresponding to the start of the experiment. b) The corresponding log-log plot of the radial distance of the intrusion front from its starting radius, R_1, as a function of the time, $t - t_1$, after the intrusion first develops in the inertia-buoyancy regime. The best-fit line to the data up to $10\,\mathrm{s}$ is shown on b) with the value and error in its slope given at the upper left on b).

In Figure 3.9, for $t \gtrsim 30\,\text{s}$, the front advanced at a slower rate as it spread in the viscous-inertia regime. Even though we are not concerned here with the rate of advance of the front in this regime, we do examine the structure of the intrusion in both the buoyancy-inertia and viscous-inertia regimes.

3.2.7 Intrusion thickness

The aim of this section is to explain how we measured the variation of the intrusion thickness as function of time, t, and position, r. Figures 3.10 and 3.11 show a snapshot with its corresponding schematic of the rightward propagating intrusion front of the same experiment shown in Figure 3.9. Vertical time series were constructed from a sequence of vertical slices taken through successive side-view snapshots of the experiment at some radius, r and time, t. We used vertical time series at $r{=}R_1$ to determine the intrusion top-to-bottom thickness, $h_1(t)$, over time at the location where the intrusion first formed (see Figure 3.11).

The intrusion thickness, h_1, at R_1 in time is shown in Figure 3.12 as computed for the experiment shown in Figure 3.5c. At early times for a short period the height of the intrusion rapidly increased then levelled off and remained constant with a mean value, $h_1 = 4.0(\pm 0.2)\,\text{cm}$, even as the intrusion front advanced in the viscous-inertia regime far beyond the buoyancy-inertia regime. This near-constant long-time value of h_1 was observed in all our experiments.

Finally, the thickness of the intrusion, $h(r,t)$, as a function of radius, r, and time, t, was computed by matching contours to side-view snapshots of the leftward and rightward propagating intrusion front at different time intervals as shown in Figures 3.5(b)-(c). Using measured values of h_f and R_{f}, we are able to demonstrate that the intrusion head adopts a self-similar structure

Figure 3.10: Side-view snapshot of rightward propagating front with $N=1.40$ s^{-1}, $\rho_0=1.020$ g/cm^3, $Q_0=7.4$ cm^3/s and $b_0=0.28$ cm at time $t=90$ s.
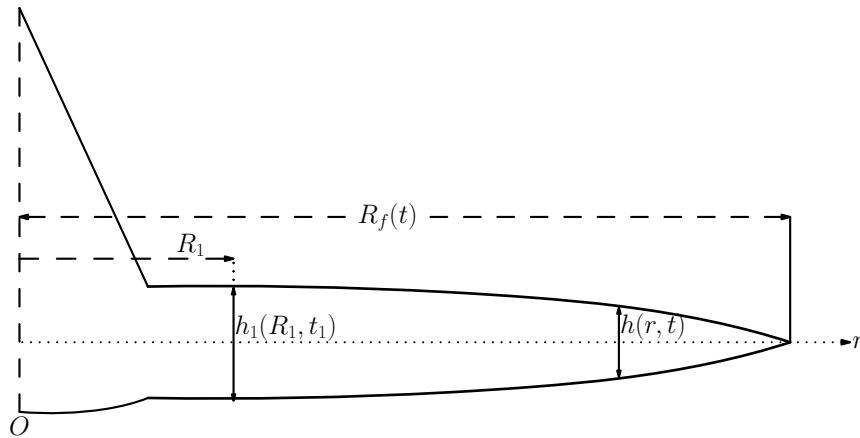
Figure 3.11: Side-view schematic of rightward propagating front shows intrusion thickness, h_1 at position, R_1 at the start of the buoyancy-inertia regime, the intrusion thickness, h, measured at radial distance, r in time, t, and the radial front position advancing in time, $R_f(t)$.

that could follow a simple power law relationship. This will be discussed in the following chapter.

3.3   Summary

In Section 3.2.6 we found the relationship between the radial distance travelled by the intrusion front position in time as $R_f - R_1 \simeq 0.94$ (± 0.01) $(t - t_1)^{0.780\ (\pm 0.004)}$ for spread in the buoyancy-inertia regime. This result is consistent with the experimental observations obtained qualitatively by Kotsovinos
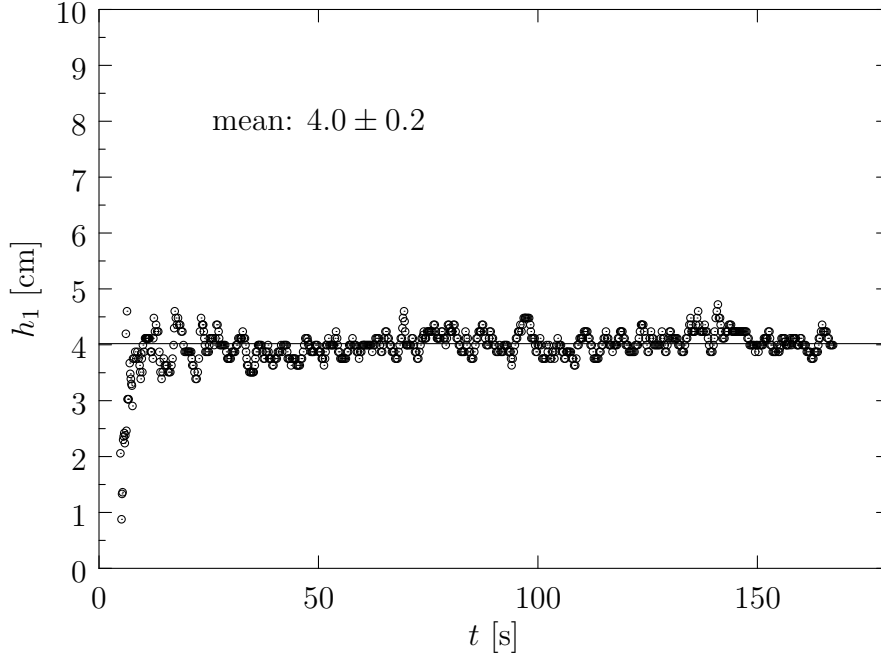
Figure 3.12: Plot of the intrusion thickness, h_1, at radial distance R_1 versus time.

(2000) and Ansong and Sutherland (2010). This was also consistent with the theory that requires a constant supply of source buoyancy flux instead of volume flux to an intrusion spreading at its neutral buoyancy level in a uniformly stratified ambient fluid.

Table 3.2 summarizes the theoretical and experimental power law relationships of the intrusion radial spread in the buoyancy-inertia regime of eight different studies. Lemckert and Imberger (1993) argued that their experimental relationship, $R_f \sim t^{0.72(\pm 0.01)}$ was consistent with the theoretical predictions of Chen (1980) disagreed with the predictions of Ivey and Blake (1985) even though $p = 0.72$ is closer to the 3/4 power law relationship.

We observed the intrusion thickness, h_1, at position, R_1, when the intrusion is first observed in the buoyancy-inertia regime. Figure 3.12 is consistent with observations for all our experiments which showed that the thickness, h_1, at R_1 is constant in time even as the intrusion spreads in the viscous-inertia

regime. This implies that the speed, u_1 at R_1, is constant. We found that the speed, u_1, computed from R_1 at t_1 ranged from 0.2 cm/s to 1.0 cm/s for all experiments.

Table 3.2: Summary of the power law relationships that give the intrusion rate of spread in the buoyancy-inertia regime as $R \sim t^P$ where p is the power or experimental exponent.

	Researchers	Assumptions	Spreading Rate
Theoretical Prediction	Chen (1980)	Constant Volume Flux	$R_f \sim t^{2/3}$
Theoretical Prediction	Didden & Maxworthy (1982)	Inertia balances Pressure Force	$R_f \sim t^{3/4}$
Theoretical Prediction	Ivey & Blake (1985)	Constant Volume Flux	$R_f \sim t^{1/2}$
Theoretical Prediction	Rooney & Devenish (2013)	Constant Buoyancy Flux	$R_f \sim t^{3/4}$
Experimental Observation	Lemckert & Imberger (1993)	Constant Volume Flux	$R_f \sim t^{0.72(\pm 0.01)}$
Experimental Observation	Kotsovinos (2000)	Inertia balances Pressure Force	$R_f \sim t^{0.75(\pm 0.05)}$
Experimental Observation	Ansong & Sutherland (2010)	Constant Buoyancy Flux	$R_f \sim t^{0.78(\pm 0.02)}$
Experimental Observation	Richards et al. (2014)	Constant Buoyancy Flux	$R_f \sim t^{0.75(\pm 0.07)}$
Volcano Observation	Holasek et al (1996)	Constant Volume Flux	$R_f \sim t^{0.65(\pm 0.01)}$

Chapter 4

Experiments: Quantitative Results

4.1 Introduction

This chapter presents the results for the measured spreading depth, Z_s, maximum depth, Z_m, the intrusion radial spread in time, $R_\mathrm{f}(t)$ and thickness, $h(r,t)$. Through theory, experiments and numerical modelling, researchers have studied the dependence of the source momentum, buoyancy and volume fluxes upon the maximum rise height of a jet, pure plume and fountain in a uniformly stratified fluid (Morton et al., 1956; Turner, 1966; List, 1979; Bloomfield and Kerr, 1998, 1999; Devenish et al., 2010). But, few have shown the dependence of these fluxes upon its spreading height (Bloomfield and Kerr, 1998).

In Section 4.2, we discuss our experimental results obtained quantitatively for the maximum and spreading depth of a forced plume with comparison to the experiments of Morton et al. (1956); List (1979); Bloomfield and Kerr (1998, 1999) and our corresponding theoretical power law relationships. Ad-

ditional quantitative results are presented in Sections 4.3 and 4.4 on the intrusion radial spread and thickness in the buoyancy-inertia regime.

4.2 Measured Maximum & Spreading Depths

This section presents the results of the measured maximum depth, Z_m, and spreading depth, Z_s, for all our experiments. First, we examine the factors that determine the maximum depth, Z_m, and the spreading depth, Z_s, of a forced plume in a uniformly stratified ambient.

The maximum depth, Z_m of a forced turbulent plume depends upon the plume source conditions (M_0 and F_0) and the ambient stratification (N). Hence, we expect the maximum depth, Z_m to scale with the jet length, H_p, and its ratio ($Z_\mathrm{m}/H_\mathrm{p}$) to depend upon the upper and lower limits of σ as shown in Figure 4.1.

For the large values of σ, a small number (two data points) of our experiments give the power law relationship

$$Z_\mathrm{m}/H_\mathrm{p} = [2.20(\pm 0.01)]\sigma^{-0.25\ (\pm 0.01)}, \quad \text{for} \quad \sigma > 50, \tag{4.1}$$

consistent with the 1/4 power for momentum-dominated source conditions.

For the smaller values of σ, the best-fit line through our data shows the power law relationship

$$Z_\mathrm{m}/H_\mathrm{p} = [4.10(\pm 0.08)]\sigma^{-0.37(\pm 0.05)}, \quad \text{for} \quad \sigma < 50. \tag{4.2}$$

This is consistent with the 3/8 exponent for buoyancy-dominated source and the proportionality relationship (2.17) given by Caulfield and Woods (1995).
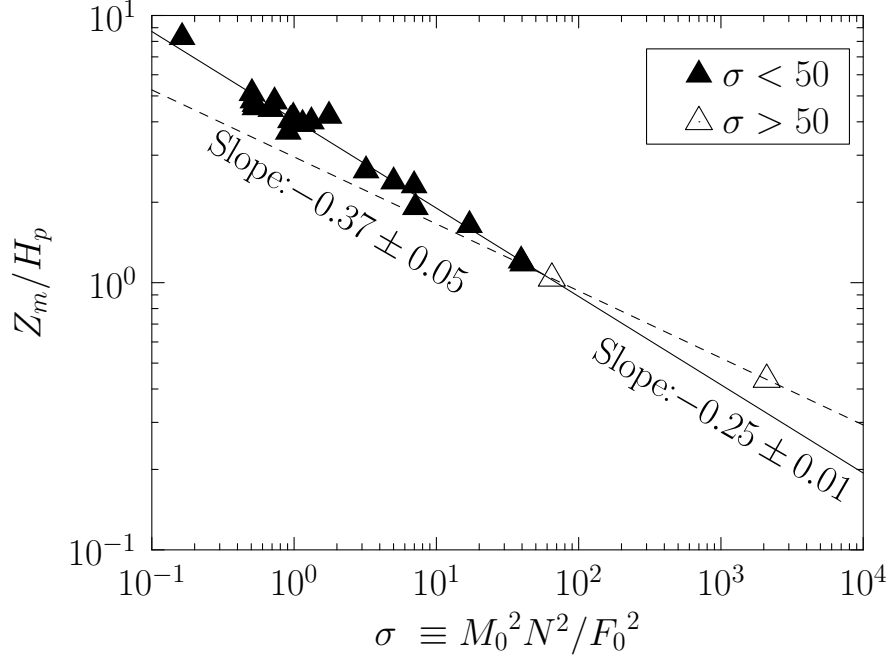
Figure 4.1: The ratio of the maximum height, Z_{m}, to the plume jet length, H_{p}, plotted against σ for all our experiments. The dashed and solid lines represent the best-fit lines computed through our experimental data for $\sigma > 50$ and $\sigma < 50$, respectively.

From these relationships: (4.2) and (4.1), we found

$$
Z_{\mathrm{m}} \simeq \begin{cases} 4.1(|F_0|/N^3)^{1/4}, & \text{for } \sigma \lesssim 50 \\ 2.2(|M_0|/N^2)^{1/4}, & \text{for } \sigma \gtrsim 50 \end{cases} , \tag{4.3}
$$

consistent with the results determined from the empirical relationship between the spreading and maximum depths given by (4.7), and (4.6).

To compare the coefficients of the maximum rise height found from our experiments shown by (4.3) with those of Morton et al. (1956), their coefficients were 40% less than the value of Z_{m} found in our experiments for both upper and lower limits of σ as given by (4.3). Their coefficients differ from ours because their source was not sufficiently turbulent to enhance mixing between the rising plume and the surrounding ambient. In their experiments, this causes the equivalent plume rising to travel further upwards before its

60

speed goes to zero, then stops at a maximum height, Z_m, and collapses back upon itself to its spreading depth, Z_s.

We may further compare our experimental results with experiments examining the maximum rise heights of jets and pure plumes in stratified fluid. List (1979) summarized the results from their experiments giving the respective empirical predictions (recast in the notation of this thesis): $Z_\mathrm{m}/H_\mathrm{p} \simeq 3.8\sigma^{-1/4}$ for $\sigma \gg 1$ and $Z_\mathrm{m}/H_\mathrm{p} \simeq 3.8\sigma^{-3/8}$ for $\sigma \ll 1$. The constant of proportionality of the maximum steady state, Z_m, (3.8) is consistent with the coefficient $4.10(\pm0.08)$ of the maximum rise height in the lower limit of σ (buoyancy-dominated) of our experiments but inconsistent with the coefficient $2.20(\pm0.01)$ for upper limit $\sigma > 50$. The large value may be attributed to the relatively small number of experiments, crude measurement methods and conversion of data to σ and H_p variables done by List (1979).

Because Z_m depends upon the plume source conditions (M_0 and F_0) and the ambient stratification, N, we expect Z_s should likewise be scaled with these parameters. We examine this dependency by plotting the ratio, Z_s/H_p (with H_p defined by (2.7)) against σ (defined by (2.12)) for all experiments. The results are shown in Figure 4.2.

For large σ, the results show that Z_s/H_p is related to σ through the power law relationship

$$Z_\mathrm{s}/H_\mathrm{p} = [1.45(\pm0.16)]\sigma^{-0.25\ (\pm0.02)}, \quad \text{for} \quad \sigma > 50, \qquad (4.4)$$

consistent with the theory for momentum-dominated source conditions. The empirical result is consistent with the experiments of Bloomfield and Kerr (1998) shown in Figure 4.2 for σ is large whether F_0 is positive or negative.

For smaller σ, the best-fit line through our data gives the power law

relationship

$$Z_{\mathrm{s}}/Hp = [2.73(\pm 0.04)]\sigma^{-0.37(\pm 0.01)}, \quad \text{for} \quad \sigma < 50. \tag{4.5}$$

This is consistent with the predicted 3/8 exponent for buoyancy-dominated source conditions. In Figure 4.2, the fit is remarkably good considering that this prediction was strictly valid only in the limit, $\sigma \ll 1$, in theory.

The experiments of Bloomfield and Kerr (1998, 2000) with $\sigma < 50$ differ significantly from ours because their source was negatively buoyant such that the source fluid collapsed to the same horizontal level of the source. If there was insufficient source momentum to allow the fountain to mix adequately with the ambient fluid, then their results would give a relationship in the lower σ range values.

Explicitly, using the relationships given by (4.4) and (4.5), we found

$$Z_{\mathrm{s}} \simeq \begin{cases} 2.73(|F_0|/N^3)^{1/4}, & M_0/F_0 \lesssim 7N^{-1} \\ 1.45(|M_0|/N^2)^{1/4}, & M_0/F_0 \gtrsim 7N^{-1} \end{cases}. \tag{4.6}$$

respectively.

In Equations (4.6) and (4.3) the power laws are consistent with expectations from the theory based upon the asymptotic limits of $M_0N/F_0 \gg 1$ and $\ll 1$.

Generally, we find that Z_{s} scales with Z_{m} as shown in Figure 4.4 which plots Z_{sv} vs Z_{mv} (the spreading and maximum depths with respect to its virtual origin) for a wide range of experiments. The plume virtual origin is situated $z_v \approx 1$ cm above the nozzle opening position at Z=0 for a downward injection. Thus, we define the distance from the virtual origin to the intrusion and maximum plume depth to be $Z_{\mathrm{sv}} = Z_{\mathrm{s}} + z_v$ and $Z_{\mathrm{mv}} = Z_{\mathrm{m}} + z_v$, respectively.
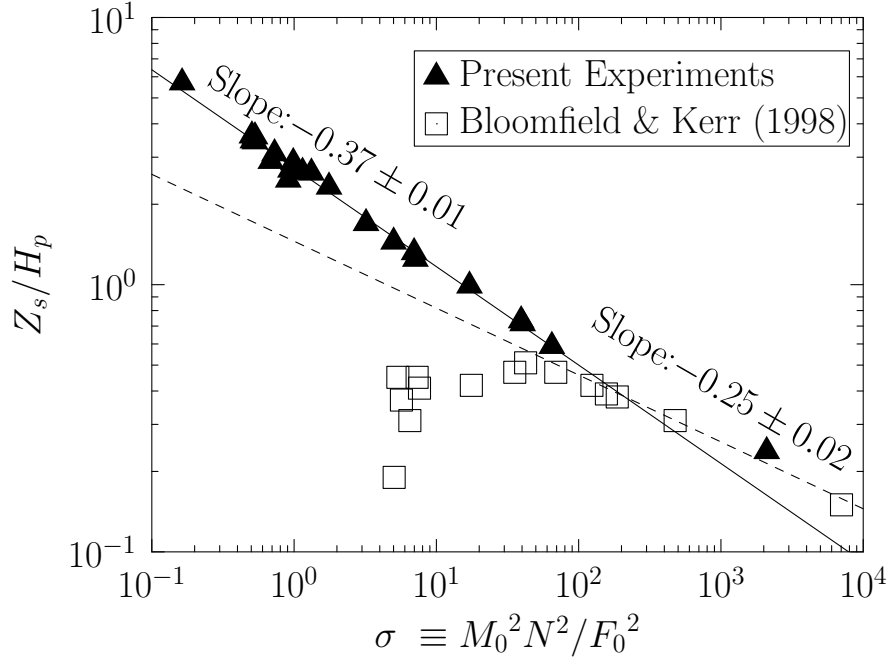
Figure 4.2: The ratio of spread height, Z_s, to plume length scale, H_p plotted against σ for all our experiments and the experiments of Bloomfield and Kerr (1998), as indicated in the legend. The dashed and solid lines represent the best-fit lines computed through our experimental data for $\sigma > 50$ and $\sigma < 50$, respectively.

The slope of the best-fit line through the data implies that the intrusion spreads at a depth,

$$Z_{sv} \simeq [0.66 \ (\pm 0.01)] \ Z_{mv}. \tag{4.7}$$

In a small number of experiments we performed with $\sigma > 50$ (open triangles in Figure 4.4), we found a moderately smaller slope of 0.5, consistent with the observations of Bloomfield and Kerr (1998) in their experiments of fountains in uniformly stratified ambient fluid.

In Figure 4.3, the ratio of Z_{sv} to Z_{mv} is plotted against the source Froude number, Fr_0, for all σ. The mean of all the points were consistent with the results shown in Figure 4.4 for both small and large σ values. For all our experiments $5 \lesssim Fr_0 \lesssim 156$ with no obvious dependence on the ratio, Z_s/Z_m.

63
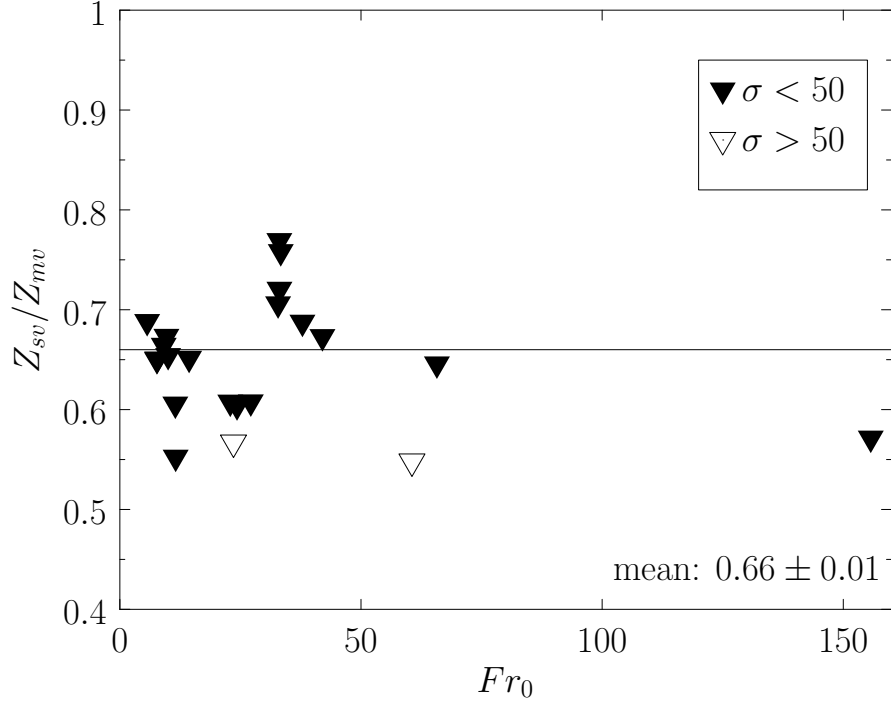
Figure 4.3: The ratio of plume virtual spread height, Z_{sv}, to virtual maximum height, Z_{mv} plotted against the source Froude number, Fr_0 for all σ in our experiments.

4.3 Measured Intrusion Radial Spread

We denote by R_0 the radius of the incident plume at Z_{s}. The radial distance from the centerline of the plume that is identified with the start of the intrusion in the buoyancy-inertia regime is called R_1. Then beyond a radius, R_v, the advance of the intrusion is dominantly influenced by a balance of viscosity and inertia.

In Figure 4.5 we plot the ratio of R_1 to R_0 for a range of experiments with different σ. The plot shows no obvious dependence of R_1/R_0 upon whether the source flow is buoyancy- or momentum-driven. An average of the data in all experiments gives

$$R_1 \simeq [3.0 \ (\pm 1.4)] \ R_0. \tag{4.8}$$

There is a lot of scatter in the data, in part as a consequence of errors in the
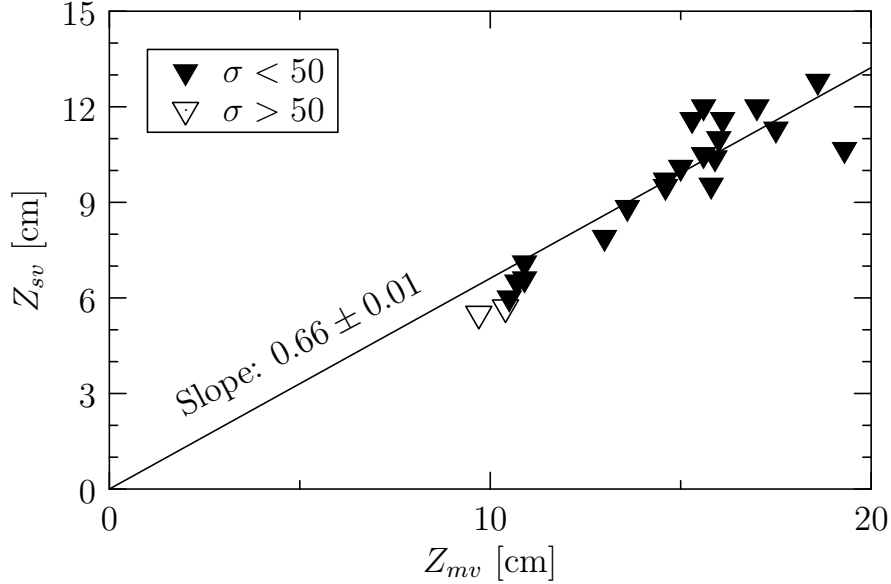
Figure 4.4: The spread depth, Z_{sv}, plotted against the maximum depth, Z_{mv}, of the fountain for experiments with $\sigma < 50$ (filled triangles) and $\sigma > 50$ (open triangles). Both depths are given with respect to the virtual origin of the forced plume. The best-fit line passing through the origin for values with $\sigma < 50$ is shown.

determination of R_0 and the statistical analysis used to determine R_1 (see Section 3.2.6). Nonetheless, our experimental results show consistency with the theoretical relationship given by Devenish and Rooney (2014).

Figure 4.6 shows the power law exponent, P_r, which determines the slope of the front position versus time of the intrusion spreading in the inertia-buoyancy regime. Explicitly, each point was computed from the slope of the best-fit line through log-log plots of $(R_f - R_1)/R_1$ versus $N(t - t_1)$ (eg see Figure 3.9). The value of the resulting power law exponent, P_r, varies between 0.6 and 0.95, but shows no obvious dependence upon σ. Averaging the results for all experiments gives $P_r \simeq 0.75(\pm 0.07)$. The large error in the exponent was dominated by statistical analysis used to determine R_1. The intercept of the best-fit line is used to find the nondimensional coefficient. This value is found to scale approximately as $L_F = (F_0/N^3)^{1/4} \; (= H_p \sigma^{-3/8})$,
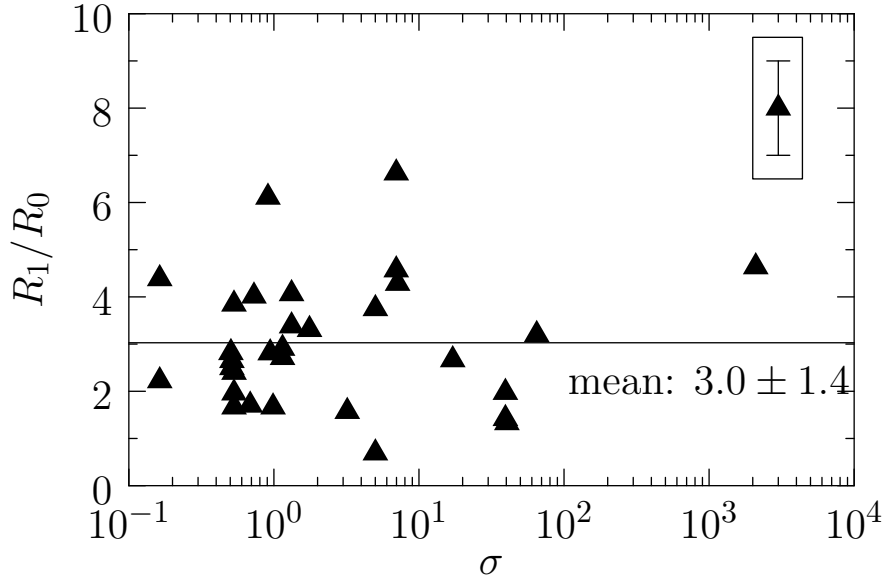
Figure 4.5: The relative intrusion starting radius, R_1/R_0 versus σ. The horizontal line shows the mean value for all σ. Typical error bars are indicated in the boxed symbol to the upper-right of plot.

consistent with the scaling predicted by (2.27). Explicitly, we find

$$R_{\mathrm{f}} - R_1 \simeq [0.33 \; (\pm 0.03)] \, L_F \, [N(t - t_1)]^{[0.75(\pm 0.07)]} \qquad (4.9)$$

In Figure 4.7 we plot the ratio of the measured and theoretical radius, $R_{\mathrm{vm}}/R_{\mathrm{vt}}$ at the start of the viscous-inertia regime for the range of σ values obtained from our experiments. The theoretical radius at the start of the viscous-inertia regime is $R_{\mathrm{vt}} = (Q_0^3/N\nu^2)^{1/5}$ as shown in Appendix 2.4 following the theoretical prediction given by Devenish and Rooney (2014). Figure 4.7 shows no obvious dependence of the ratio, $R_{\mathrm{vm}}/R_{\mathrm{vt}}$, upon σ and the data points are scattered. But, the mean of all the data points gives

$$R_{\mathrm{vm}} \simeq [0.9 \; (\pm 0.2)] \, R_{\mathrm{vt}} \qquad (4.10)$$

which shows that the measured radius at the start of the viscous-inertia

66
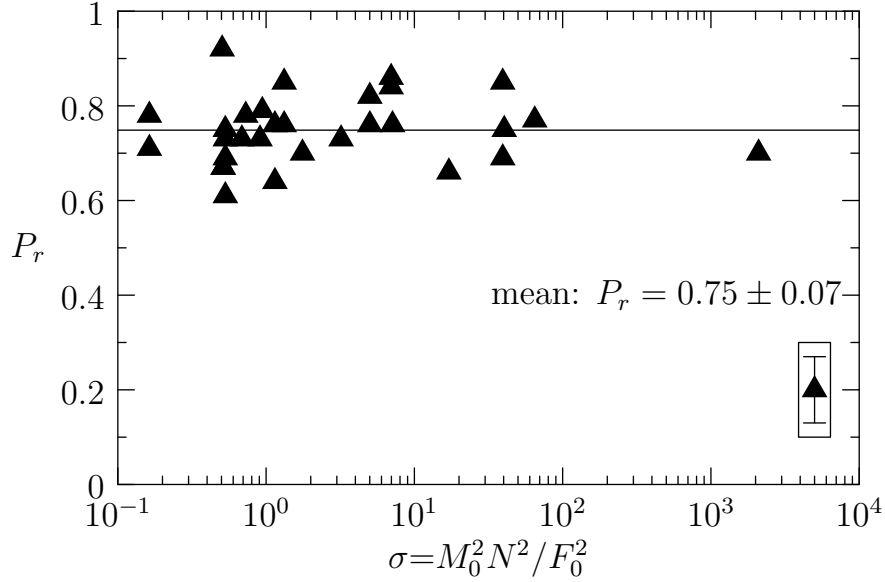
Figure 4.6: The best-fit power law exponent, P_r, for the intrusion front position versus time plotted versus σ. Explicitly, P_r appears in the relation $\Delta R_\mathrm{f} \propto \Delta t^{P_r}$ with $\Delta R_\mathrm{f} \equiv R_\mathrm{f} - R_1$ and $\Delta t \equiv t - t_1$. A typical error bar is indicated in the lower right-hand corner of the plot. The mean value of all data is indicated by the horizontal line.

regime is consistent with the theory in (2.42) (Devenish and Rooney, 2014) used to predict the starting radius, R_v. This theoretical derivation is outlined in Appendix 2.4.

4.4   Measured Intrusion Thickness

For given R_1 in each experiment, we measure the corresponding intrusion thickness, h_1, $(h_1(t))$ at this location found to be constant in time. As in the case shown in Figure 3.12, we find that h_1 is approximately constant in time shortly after the intrusion becomes established.

The values of h_1 computed from a range of experiments are plotted in Figure 4.8. Here, h_1 is normalized by H_p and plotted against σ. The error associated with h_1/H_p is of the order 0.01, much smaller than the measured values. The log-log plot clearly shows that the intrusion depth gets smaller
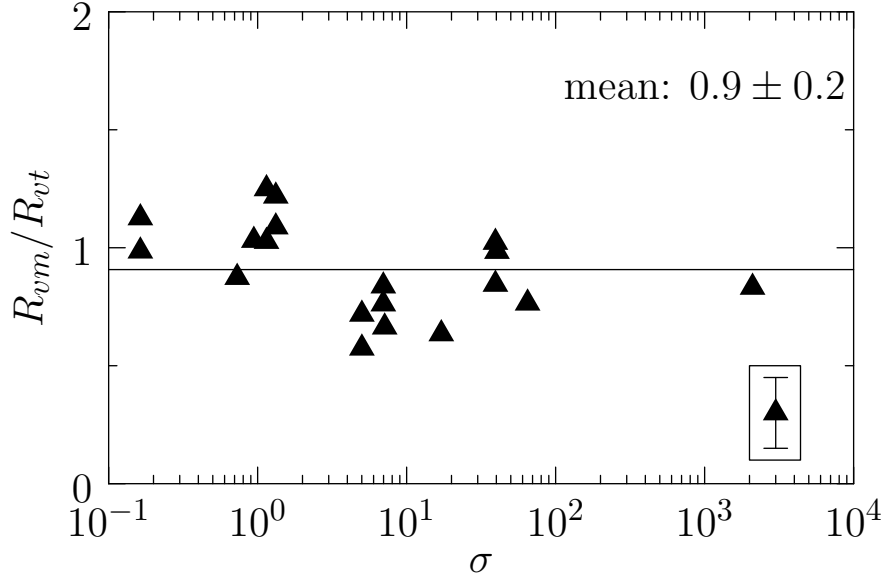
Figure 4.7: The relative intrusion measured and theoretical starting radius, R_{vm}/R_{vt}, in the viscous-inertia regime versus σ. The horizontal line shows the mean value for all σ. Typical error bars are indicated in the boxed symbol to the lower-right of plot.

with increasing σ. Explicitly, for $\sigma < 50$, we find

$$h_1 = H_p[1.36\ (\pm 0.06)]\, \sigma^{-0.30\ (\pm 0.02)}. \tag{4.11}$$

The exponent is -0.30, is found by finding the best-fit line through all the points. For $\sigma \ll 1$, we expect the source momentum flux, M_0, should not play a role, and like Z_{sv}, we expect h_1, to scale as $H_p\sigma^{-3/8} = (F_0/N^3)^{1/4}$ independent of M_0. It may be that errors associated with the measurement of h_1 could explain the discrepancy. Indeed, the solid line of slope $-3/8$ in Figure 4.8 indicates that the value of h_1 in experiments with low σ are not inconsistent with the $-3/8$ power.

We now consider the shape of the intrusion. Figure 4.9a shows profiles of the intrusion thickness, $h(r;t)$, as a function of radial distance, r, determined from side-view snapshots of the experiment shown in Figure 3.5. The profiles
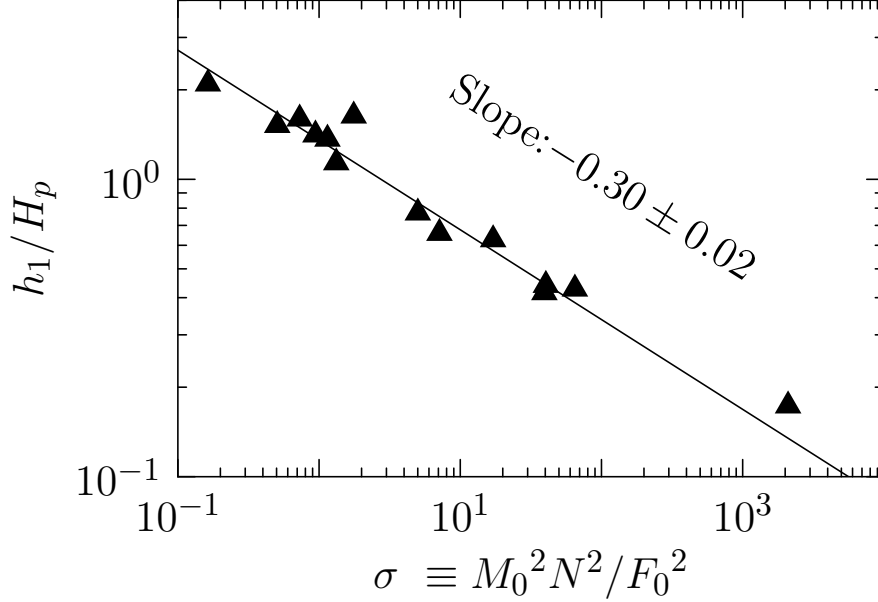
Figure 4.8: The intrusion thickness at R_1 relative to H_p versus σ. The best-fit line through all the points is shown.

are plotted only for times $t=16, 24, 38, 48\,\text{s}$. Generally, we found that the thickness of the intrusion decreased with increasing radius, but the thickness at R_1 changed little over time, consistent with Figure 4.9.

Having computed the values of h_1 and R_1, and knowing the front position as a function of time, $R_f(t)$, we define a rescaled nondimensional height by $\tilde{h}=h/h_1$ and a rescaled nondimensional radial coordinate by $\tilde{r}=(R_f-r)/(R_f-R_1)$ as shown in Figures 4.9(b) and 4.10. The data shown in Figure 4.9 suggests that the intrusion structure is self-similar, but with constant thickness, $h=h_1$, at $r=R_1$.

Generally, we find that the rescaled profiles of $\tilde{h}(\tilde{r};t)$ computed for a wide range of times collapse reasonably well onto a single curve. This is illustrated in Figure 4.10, which shows the rescaled data from Figure 4.9b on a log-log plot. The data collapses onto an almost straight line. A best-fit line through the log-log plots of the four curves gives a power law of the form, $\tilde{h} \propto \tilde{r}^{P_h}$, satisfying $\tilde{h}(0)=0$ and $\tilde{h}(1)=1$.

69
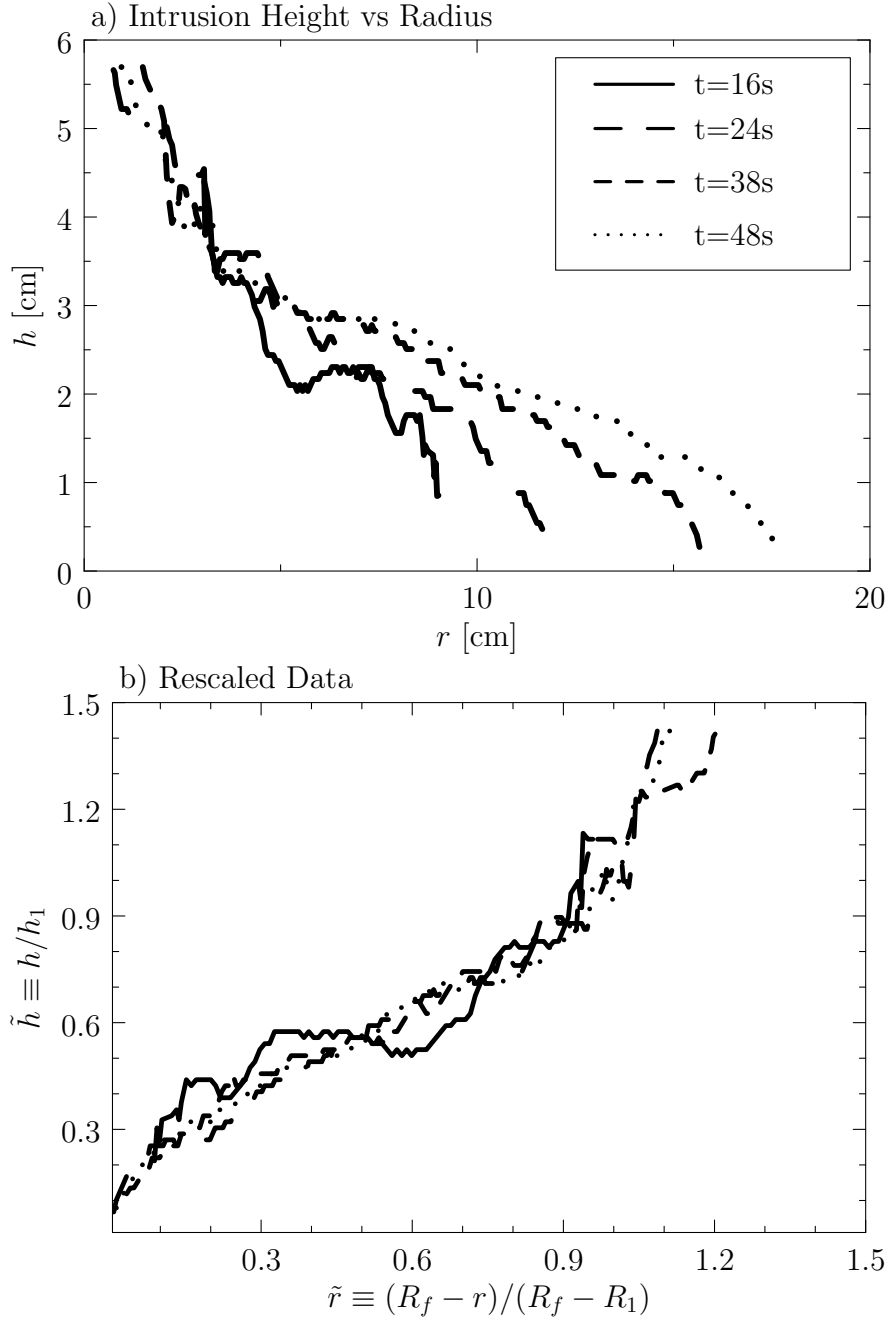
Figure 4.9: a) Plot of the intrusion thickness, h, as a function of radial distance, r, for times $t = 16, 24, 38, 48$ s. b) Corresponding plot of the normalized height, $\tilde{h} = h/h_1$ versus the normalized radius, $\tilde{r} = (R_f - r)/(R_f - R_1)$. Results are computed for the same experiment shown in Figure 3.5.

Figure 4.11 shows that the power law exponent, P_h, does not vary significantly with σ. Its value computed for six different experiments with σ ranging from 1 to 2100, is $P_h \simeq 0.55$ (± 0.03) with error computed from the

Log-log of Rescaled Data
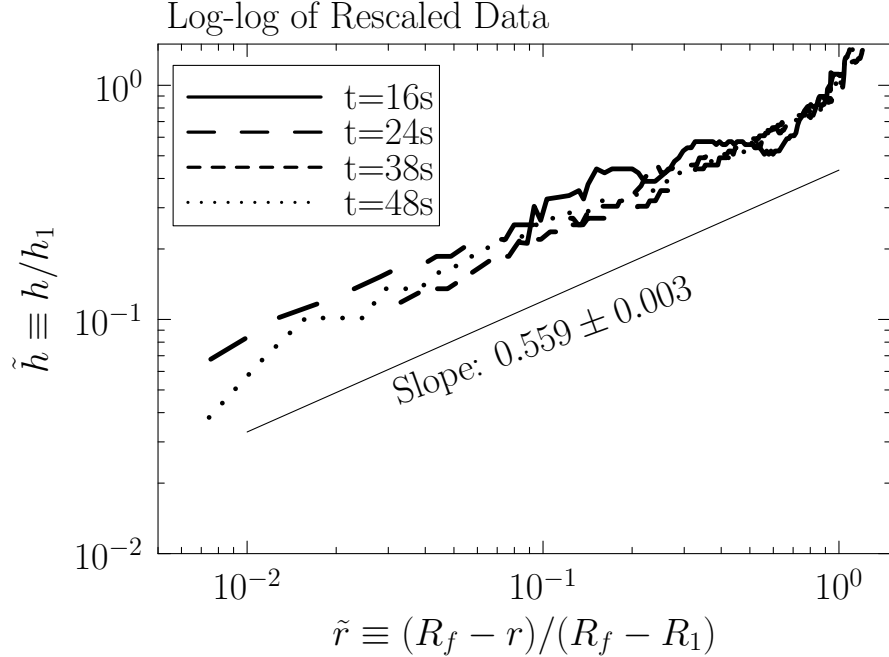
Figure 4.10: Log-log plots of the normalized height, $\tilde{h} = h/h_1$ versus the normalized radius, $\tilde{r} = (R_f - r)/(R_f - R_1)$ computed for the same experiment shown in Figure 4.9(b). The solid diagonal line is the vertically offset best-fit line through the four collapsed curves.

six data points showing the upper and lower ranges of P_h. These six experiments were chosen based on their relatively small statistical error found from corresponding data points of $\tilde{h}$ versus $\tilde{r}$ as shown in Figure 4.10.

Explicitly we find the relation

$$\frac{h}{h_1} \sim \left(\frac{R_f - r}{R_f - R_1}\right)^{0.55(\pm 0.03)}. \tag{4.12}$$

This empirical result supports the theoretical assumption that the intrusion thickness as a function of radius may be represented by (2.29). However, a consequence of this assumption, together with assumptions that the volume or buoyancy flux is constant, is that the intrusion front should advance linearly in time near the source and as the square root of time in the far field (2.36). With $P_h \simeq 0.55$, the transition between these asymptotic regimes is

71
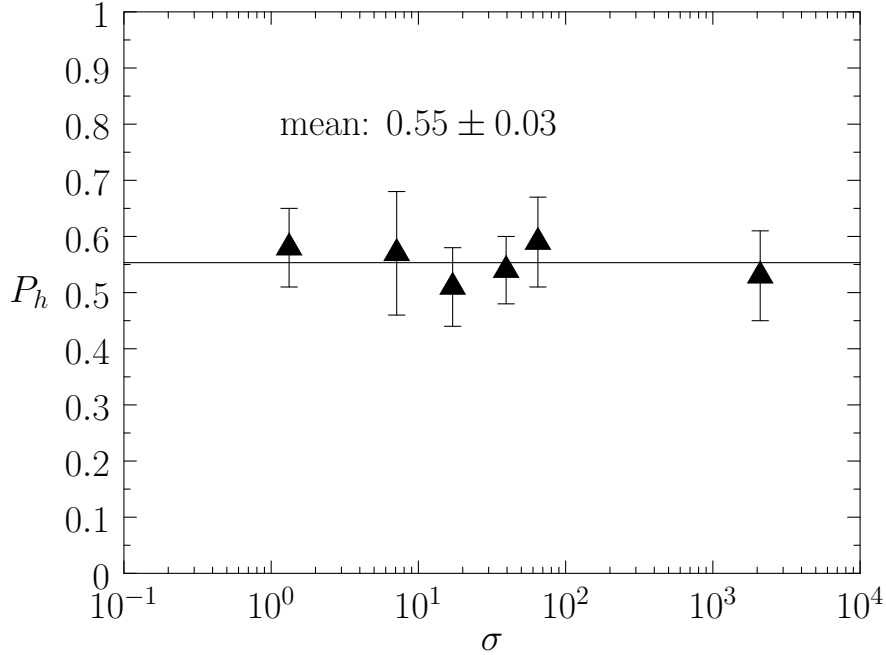
Figure 4.11: Power law exponent, P_h, of rescaled intrusion height profile determined in experiments with six values of σ.

predicted to occur at radius $R_{fc} \simeq 4.1R_1 \simeq 12R_0$ for $R_1{=}3R_0$.

In our experiments, the buoyancy-inertia regime was observed to extend for $R_1 \lesssim R_f \lesssim 10R_{fc}$ (eg see Figure 3.9). In light of this observation and the fact that the power law fits resulted in the exponent found in Figure 4.6, it is still unclear that the intrusion front position truly advances as a 3/4 power of time in the buoyancy-inertia regime. Possibly as given by (2.36), the intrusion front could advance more quickly at early times and more slowly in the inertia-buoyancy regime at later times. But from the inherent noise created from these experiments after analysis, this did not allow us to observe such transition, if indeed it exists.

Chapter 5

Applications

Environmental applications of forced turbulent plumes in uniformly strati-
fied ambient fluid include large volcanic eruptions spreading in stratosphere
of such is the June 15, 1991 Mount Pinatubo eruption and deep ocean oil
blowouts such as the April 20, 2010 Gulf of Mexico Deepwater Horizon oil
spill.

5.1   Application to Supervolcanoes

Despite the uncertainties in our experimental results, it is a useful exercise to
consider how our results apply to observed volcanic explosions that extend
well into the stratosphere and are not significantly affected by background
winds and the Earth's rotational force for the first few hours of its radial
spread. A large volcanic plume can penetrate tens of kilometers into the
stratosphere (Koyaguchi and Tokuno, 1993; Koyaguchi, 1994; Holasek et al.,
1996b; Baines and Sparks, 2005). It then collapses and ultimately spreads
as an intrusion with thickness (Sparks et al., 1986; Baines and Sparks, 2005)
ranging from $1\,\mathrm{km}$ to $2\,\mathrm{km}$. The umbrella clouds thickness over such rela-
tively small vertical distance in the stratosphere we can effectively apply the

73

Boussinesq approximation.

5.1.1   Mount Pinatubo Eruption

In the extreme case of the June 15, 1991, Mount Pinatubo eruption, satellite observations revealed (Holasek et al., 1996b) that the eruption column extended upwards to a maximum height of $Z_{\mathrm{m}} \sim 40\,\mathrm{km}$. With the radius of the eruption column at its source taken to be on the order $b_0 = 1\,\mathrm{km}$, the virtual origin was estimated to be approximately $4\,\mathrm{km}$ below the surface (Holasek et al., 1996b). Thus, using (4.7), we estimate the intrusion should have spread around $25\,\mathrm{km}$ altitude consistent with the model-predicted neutral buoyancy height, $Z_{\mathrm{s}} \simeq 24\,\mathrm{km}$ (Baines and Sparks, 2005).

The momentum and buoyancy fluxes across the tropopause provide the initial conditions for the plume entering the stratosphere (Ansong and Sutherland, 2010). If we assume that the buoyancy flux dominates over the momentum flux at the tropopause (near $16\,\mathrm{km}$ altitude), then taking $N = 0.017\,\mathrm{s}^{-1}$ in the stratosphere (Holasek et al., 1996b) and using (4.6), we estimate the buoyancy flux at the virtual origin to be $F_0 = 1.2 \times 10^{11}\,\mathrm{m}^4/\mathrm{s}^3$. Assuming the stratification of the troposphere is negligible, this would also be the buoyancy flux at the tropopause. If the momentum flux dominates, we find $M_0 = 2.9 \times 10^{13}\,\mathrm{m}^4/\mathrm{s}^2$ consistent with predicted flux at the caldera of the order $10^{14}\,\mathrm{m}^4/\mathrm{s}^2$ (Holasek et al., 1996b). Typically in the stratosphere the buoyancy frequency varies between an order of $10^{-2} - 10^{-3}\,\mathrm{s}^{-1}$ (Holasek et al., 1995). But during the Mount Pinatubo eruption the stratospheric stratification was found within the ranges of $0.012\,\mathrm{s}^{-1}$ and $0.017\,\mathrm{s}^{-1}$ (Holasek et al., 1995). Between this variation the momentum flux is still of the order $10^{13}\,\mathrm{m}^4/\mathrm{s}^2$.

Assuming the buoyancy flux is negligible, this would also be the momen-

tum flux at the tropopause. Below we will see that observations of the intrusion speed and thickness, imply that the eruption was, in fact, momentum-dominated at the tropopause.

5.1.2   Radial Spreading Umbrella Cloud

The umbrella cloud emanating from the Mount Pinatubo eruption was observed to propagate radially away at a speed as fast as $u_1 \simeq 20$ m/s near the start of the inertia-buoyancy regime (Holasek et al., 1996b). This surpassed the local stratospheric wind speeds, so that ambient winds did not significantly affect the intrusion evolution at least during the early stages of its propagation in the buoyancy-inertia regime. Indeed, the spread was observed to be symmetrical about the eruption column for the first 4-5 hours over which time it spreads radially 300 km from the source (Holasek et al., 1996b).

Taking $N = 0.017 \, \text{s}^{-1}$ and the speed, $u_f = 20$ m/s, of the intrusion front in (2.18) (Holasek et al., 1996b), with Fr = 0.3 gives an estimate for the intrusion thickness of $h_1 \simeq 4$ km. This is consistent with the observed thickness (Koyaguchi, 1994) that ranged between 3 km and 6 km.

The first satellite observation of the Pinatubo eruption was estimated to be made 800 s after the initial explosion at 1341 (Holasek et al., 1996b). At this time the mean radius of the umbrella cloud was approximately 30 km. We take this as the value of R_1 which, using (4.8), is consistent with the estimated radius of the central eruption column, $R_0 \simeq 10$ km.

The volume flux at R_1 is estimated to be $Q_i = 2\pi R_1 h_1 u_1 \simeq 1.5 \times 10^{10}$ m^3/s, which is of the order 5×10^{10} m^3/s estimated indirectly by observations from satellite images (Koyaguchi, 1994). Using (2.23), the radial buoyancy flux associated with the intrusion is $F_i = Q_i N^2 h_1 \simeq 1.7 \times 10^{10}$ m^4/s^3.

Comparing these results with the above estimated values of F_0 and M_0 for plumes dominated buoyancy-flux and momentum-flux respectively, we see that F_0 is only moderately larger than F_i. If the flow was buoyancy dominated at the tropopause, we would expect significantly reduced buoyancy flux associated with the intrusion: $F_0 \gg F_i$. Therefore, we expect that the plume was momentum-dominated with $M_0 \simeq 2.9 \times 10^{13} \text{ m}^4/\text{s}^2$ at the tropopause, situated at $z \simeq 16 \text{ km}$.

Observations of the Pinatubo plume spread (Holasek et al., 1996b) indicate that the radius increased as $t^{0.65(\pm 0.01)}$ for distances out to 600 km (see Table 3.2). The power law is consistent with the box-model prediction (2.21) assuming a constant volume flux, Q_i. But, it differs from our experimental results that show on average the intrusion radius increases as $t^{0.75(\pm 0.07)}$. This may be an indication that the scatter in our estimate of the power law is insufficient to state conclusively that the intrusion advance is closer to a (buoyancy conserving) 3/4 power law instead of a (volume conserving) 2/3 power law. Given that the entrainment of ambient air into the Pinatubo umbrella cloud was evident from photographs, it seems unlikely that this intrusion could be well-modelled as having a constant volume flux at radius, R_1. One reason for the discrepancy could be that R_1 (and t_1) were incorrectly estimated from satellite observations. Alternately, it may be that particles in the flow subsequently alter the buoyancy flux within the umbrella cloud.

The measured parameters (intrusion speed, radius, thickness) from our experiments of forced turbulent plumes in uniform stratification are extremely small when compared with the corresponding measured satellite data of Mount Pinatubo volcanic eruption spreading in the stratosphere. To scale experiments correctly with such real life occurrences, we used σ given by (2.12). The experiments discussed explore both large and small values of σ covering

76

a wide range of values from 1 to 2100. For the Mount Pinatubo eruption σ was found to be approximately 18, hence, our experiments were suitable to apply to the Mount Pinatubo eruption having known that our experiments have covered this range of σ values.

The results of our experiments may be applicable to other volcanic eruptions spreading in the stratosphere upon meeting the following criteria:

- strong volcanic plumes that rise above the tropopause well into the stratosphere

- collapses and spreads radially as an intrusion in the stratosphere

- eruption column spread within the first few hours is unaffected by Coriolis forces

- negligible wind advection during the period of the umbrella cloud spread

5.2 Application to Gulf of Mexico Oil Spill

We also consider the application of our results to the spreading of oil at its some depth of such is the 2010 Deepwater Horizon blowout in the Gulf of Mexico. Crudely modelling the source as jet with opening on the scale of $b_0 = 0.1$ m and volume flux 0.1 m^3/s (about 55000 barrels per day), the source momentum flux is of the order $M_0 \sim 1$ m^4/s^2. Further assuming the stratification of the ocean at depth is of the order $N \sim 10^3$ s^{-1}, (4.6) predicts a spreading height around $Z_s = 50$ m above the source. In fact, observations revealed that the oil from the plume spread laterally $200 - 500$ m above the source (Camilli et al., 2010; Adcroft et al., 2010). The discrepancy is attributed to the multiphase dynamics (example gas bubbles, oil droplets, gas hydrates) of the plume, which significantly change the buoyancy of deep

water oil spills throughout the whole evolution of the rising jet, collapsing fountain and spreading intrusion (Yapa and Zheng, 1997).

Chapter 6

Summary and Conclusion

This research presented the characteristics of forced turbulent plumes in a uniformly stratified ambient fluid with constant stratification. We have examined the spreading depth, Z_s, the radial advance, $R_f(t)$, and thickness, $h(r, t)$, of a radial intrusion resulting from the collapse of a forced plume at its neutral buoyancy level. The motivation for this study has been to extend the understanding of the dynamics of turbulent plumes rising and spreading in the stratosphere. We have applied our results to the Mount Pinatubo volcanic eruption and extended this application towards the 2010 Gulf of Mexico oil spill.

A section of this study was extended to predict the spread and maximum heights given as a function of the ambient stratification, source momentum and buoyancy fluxes of a forced turbulent plumes shown by (4.6) and (4.3) respectively. The power laws of these equations follow the expectations from the theory based upon the asymptotic limits of $M_0 N / F_0 \gg 1$ and $\ll 1$.

The resulting intrusion thickness, h_1, at R_1 for all experiments was found constant in time for spreading up to the viscous-inertia regime. In addition, the overall thickness of the intrusion evolving in position and time (see Figure

4.9) followed a self-similar shape predicted by (4.11). This does not follow the box-model approach of shallow water theory which assumes the intrusion with uniform thickness, h, that only evolves in time (Ungarish and Zemach, 2012; Ungarish, 2009).

In Chapter 2, Section 2.3.1, the theory predicts the intrusion radial front position in time as $R_f - R_1 \sim (t - t_1)^{2/3}$ assuming a constant source volume flux. This theoretical prediction was not found consisted with the intrusion radial spread in time measured in our experiments. Instead, our results showed consistency with the theory for 3/4 power law. This is also consistent with other experiments (Didden and Maxworthy, 1982; Kotsovinos, 2000) and theory that requires constant buoyancy flux instead of the volume flux of an intrusion spreading in uniformly stratified fluid.

However, the self-similar shape of the intrusion shown by (4.12), together with the observed restriction that the intrusion thickness is fixed in time at its source, dictates according to (2.36), that the intrusion speed should first advance linearly in time and then as the square-root of time. Given the power law exponent determining the head shape was $P_h \simeq 0.55$, the transition from linear to square-root dependence is predicted to take place when the front position is at $R_f \simeq 4R_1$. This transition position is in the middles of the range of R_f over which the power law exponent P_r was determined. And so, it is unclear if the assumption whether the intrusion exhibited self-similar behaviour resulting from a constant buoyancy flux as in the approximations leading to (2.27), or whether it exhibited a transition from near-to-far plume evolution as in (2.36).

Both predictions assumed a constant source buoyancy flux of the intrusion at $r = R_1$, but this may not be the case. The theories presented here have ignored the modification of the ambient stratification and opposing velocities

induced by the radially advancing intrusion. Such radially-inward motions of enhanced stratification could modify the entrainment associated with the fountain and so change the source conditions for the intrusion. Much larger scale experiments and more sophisticated analyses are required to address these issues.

Measurement of the density variation across the intrusion spread at radial distance, R_1, with corresponding thickness, h_1, would provide additional information on the radial spread of the intrusion in time. Likewise, the density variation at a point on position, R_1 would also make sufficient justification on what relationship correctly predicts the spread of the intrusion as the density variation at this position is unknown but assumed to be constant in theory.

In our experiments we measured the density across the radial spreading intrusion top-to-bottom height at radius, R_1, using the traversing conductivity probe. The vibrations of the probe as it traverses through the spreading intrusion did not allow us to observe whether the intrusion density at R_1 was the same as the ambient density at this height or there was a slight variation in its density because of the inherent noise in the data. However, the density profiles of the stationary ambient measured by the traversing conductivity probe and densitometer were consistent for corresponding experiments.

6.1   Future Work

The experiments conducted for this research study did not involve many complications of real volcanic explosion that extend into the stratosphere such as the pressure of particles, wind shear, and temperature. But the dynamics of radially spreading intrusions created from turbulent plumes in stratified ambient fluids were adapted to gain meaningful insights. Further

studies could be conducted to investigate particle-laden plumes and azimuthal instability as outlined below.

6.1.1 Particle-Laden Plumes

The effects of particles in the rise and spread of turbulent plumes in stratified fluid could provide useful information on the spread of volcanic plumes in the stratosphere.

This has further application to supervolcanoes spreading in the stratosphere. Experiments could be done with fresh water fluid mixed with particles injected vertically upwards into stratified fluid. Different size particles could be used by analogy with the problem investigated by Carey et al. (1986) who conducted experiments varying the flow rate, particle size and concentration.

The variation of particle size in each experiment of a forced plume rise and spread could be conducted with all other parameters constant which includes the particle concentration. From such experiments the maximum penetration height, steady state height and spread height could be measured with the variation of differently sized particles. Additionally, the radial spread of the intrusion in time could be measured to understand quantitatively how differently sized particles could affect the spread of such intrusions.

Alternatively, Zarrebini and Cardoso (2000) has conducted particle-laden experiments from which they used sampling trays positions along the tank floor to collect the particles falling out of the plume. From this the deposition of particle fall-out at specific horizontal positions away from the source along the floor of the tank was measured.

The deposition and concentration of particles as the plume rises and spreads in a uniformly stratified ambient fluid could be measured at different radial distances from the source along the tank floor similar to the prob-

lem of Zarrebini and Cardoso (2000) but without the use of trays positioned at specific distances away from the source. Such experiments would require sophisticated laboratory design and equipment.

6.1.2 Azimuthal Instability of Forced Plumes in Stratified Environments

The experimental results in Chapter 3, Figure 3.6 showed that the radial spread of an intrusion as observed from a top view is not axisymmetric. As a result, analysis of these experiments were done from side-view to reduce the influence of thin regions of mixing shown as lighter intensity variations along the edges of the intrusion front position created from the azimuthal instabilities. Azimuthal instabilities occur as a consequence of the interaction between the radial spreading intrusion head height and the stratified interface ahead of the intrusion front. These disturbances became obvious as they grow with the intrusion front position in time with spreading beyond the buoyancy-inertia regime. As the vertical extent of the intrusion head decreases with radial distance traveled it becomes comparable with the stratified interface. Further experiments and analyses could be use to observe the growth of these instabilities as the intrusion evolves in position and time.

Instability created in the radial spread of an intrusion emanating from the origin of a forced plume at its neutral buoyancy level is not well understood in this nature and may greatly impact the rate of spread of the intrusion front position in time.

Appendix A

Plumes in uniform ambient fluids

A.1 Entrainment Hypothesis

The entrainment hypothesis Morton et al. (1956) postulates that the speed, u_e, of laterally entrained ambient fluid across the plume interface is proportional to the plume vertical velocity, $w(z)$,

$$u_e = \alpha w(z), \qquad (A.1)$$

where α is the coefficient of entrainment given by a constant value that is different for fountains, jet- and plume-like flows. Theoretical and experimental studies have predicted that $\alpha_f = 0.085$ for fountains (Bloomfield and Kerr, 1998), $\alpha_j = 0.076$ for jets (List, 1979), $\alpha_p = 0.12$ for plumes with top-hat profile (List, 1982), but α_p could vary between 0.10 (Baines, 1983) and 0.16 (Shabbir and George, 1994) where the 60% variation has been shown to have an effect on its ability to predict the fluxes at any given height (Kaminski and Carazzo, 2005).
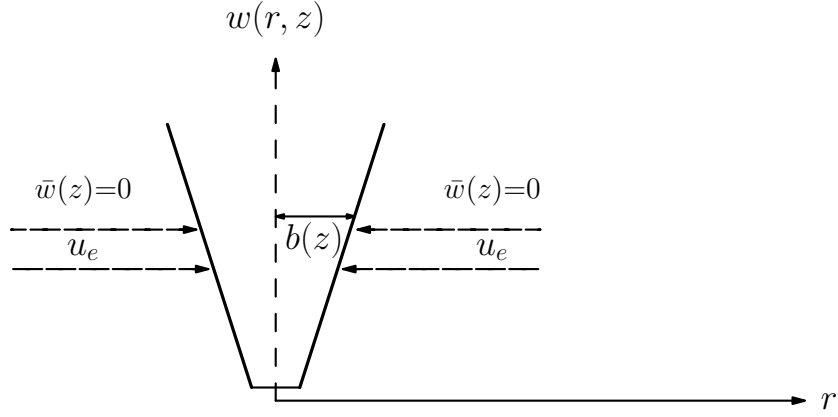
Figure A.1: Schematic diagram of fluid entrainment into the plume where b is the plume radius.

From this hypothesis Morton et al. (1956) derived the equations for the plume evolution from the laws of mass, momentum and energy conservation using the top-hat profile. These equations are summarized and discussed in the following sections.

A.2   Top-Hat Profile

The top-hat profile dictates that the velocity and density inside the plume across its horizontal level is uniform/constant and zero outside:

$$w(r, z) = \begin{cases} \bar{w}(z) & \text{for } r \leq b \\ 0 & \text{for } r > b \end{cases}. \tag{A.2}$$

$$g'(r, z) = \begin{cases} \bar{g}'(z) & \text{for } r \leq \imath b \\ 0 & \text{for } r > \imath b \end{cases}. \tag{A.3}$$

where $\bar{w}(z)$ and $\bar{g}'(z)$ are the vertical velocity and density ($\imath \approx 1$) of equal distribution inside the plume (Morton, 1959) (see Figure A.1).

For the velocity is constant inside the plume, the density is also constant.

A.3   Volume Flux

A fluid of density, ρ, is injected vertically upwards from an effective point source into a heavier surrounding ambient fluid, travels vertically upwards in time, t, as its momentum and buoyancy fluxes decrease to zero. For this flow the continuity equation is given by

$$\frac{\partial \rho}{\partial t} = -\nabla \cdot (\rho \underline{u}), \tag{A.4}$$

where ∇ is the operator and $\underline{u} = (u, v, w)$ is the velocity field. From the product rule (identity) of a scalar and vector ρ and $\underline{u}$, respectively, its divergence is given by

$$\nabla \cdot (\rho \underline{u}) = \rho(\nabla \cdot \underline{u}) + \underline{u} \cdot (\nabla \rho). \tag{A.5}$$

Assume the flow is incompressible and the plume vertical motion is steady or statistically independent of time, (A.4) is reduced to the non-divergent velocity field,

$$\nabla \cdot \underline{u} = 0. \tag{A.6}$$

For the plume vertical structure is cylindrical in shape (Figure A.2), we apply the Gauss's (also called the Divergence) theorem that converts the integral of the divergence $(\nabla \cdot \underline{u})$ over the plume volume into the flux integral of $\underline{u}$ over the surfaces that bound the volume:

$$\int_V (\nabla \cdot \underline{u}) dV = \oint_S \underline{u} \cdot \widehat{n} ds, \tag{A.7}$$

where $\widehat{n}$ is a unit vector. In Figure A.2, the inward vertical flow and entrainment along the sides are positive and in the opposite direction of $\widehat{n}$. But, the total outward vertical flow is in the same direction of $\widehat{n}$. It follows that the

86
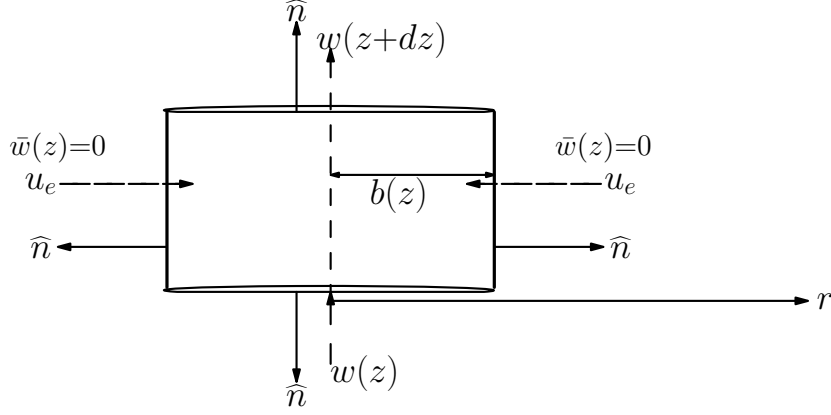
Figure A.2: Schematic diagram of of plume with cylindrical shape.

total flux is given by the amount of fluid passing through all the surfaces that bound the plume per unit time:

$$u_e(2\pi b)dz = w(z+dz)(\pi b^2)dz - w(z)(\pi b^2)dz. \qquad (A.8)$$

Given that the rate of entrainment is $u_e = \alpha w$, (A.8) forms the volume flux,

$$\frac{d(w\pi b^2)}{dz} = 2\pi \alpha b w. \qquad (A.9)$$

A.4   Momentum Flux

Using the momentum conservation equation as

$$\frac{D\underline{u}}{Dt} = \frac{\partial \underline{u}}{\partial t} + \underline{u}.\nabla\underline{u} = -\frac{1}{\rho_0}\nabla p + g\frac{\Delta\rho}{\rho_0}\hat{z}. \qquad (A.10)$$

Assume a steady incompressible flow within the boundary of the plume, the momentum conservation equation is reduced to

$$\underline{u}.\nabla\underline{u} = -\frac{1}{\rho_0}\nabla p + g'\hat{z} \qquad (A.11)$$

87

where $g' = g(\Delta\rho/\rho_0)$ is the reduced gravity. The pressure is negligible given that the vertical height over which the plume rises is significantly larger than the plume width with high vertical motion along the plume centreline and slower motion along the side, hence A.11 is reduced to

$$\underline{u}.\nabla\underline{u} = g'\hat{z}. \tag{A.12}$$

Applying using incompressibility, the left-hand side becomes $\nabla.(\underline{u}\underline{u})$ and the Divergence theorem gives

$$\int_V g'\hat{z}dV = \oint_S ((\underline{u}\underline{u}) \cdot \widehat{n})ds. \tag{A.13}$$

Taking the vertical component and integrating over a slab of depth, dz, gives

$$\frac{d(\pi b^2 w^2)}{dz} = \pi b^2 g'. \tag{A.14}$$

A.5   Buoyancy Flux

Using the conservation of internal energy equation as

$$\frac{D\rho}{Dt} = \frac{\partial\rho}{\partial t} + \nabla \cdot (\rho\underline{u}) = -w\frac{d\bar{\rho}(z)}{dz}. \tag{A.15}$$

where ρ is the total density (mean and perturbation) and $\bar{\rho}(z)$ is the ambient density change with height. Assuming a steady incompressible flow inside the plume, (A.15) becomes

$$\nabla \cdot \underline{u} = -\frac{w}{\rho}\frac{d\bar{\rho}(z)}{dz}. \tag{A.16}$$

For the ambient stratification given by (2.10), we rewrite (A.16) as

$$\nabla \cdot \underline{u} = \frac{wN^2}{g'}.$$

(A.17)

Multiple both sides of A.17 by the reduced gravity, g', we obtained

$$\nabla \cdot (g'\underline{u}) = wN^2,$$

(A.18)

where the density change between the plume and ambient varies position.

From Figure A.2, we apply the Divergence theorem to (A.17) as

$$\int_V wN^2 dV = \oint_S g'(\underline{u} \cdot \widehat{n}) ds,$$

(A.19)

For the inward flows along the side and bottom surfaces are in the opposite direction of $\widehat{n}$ and the outward flow is in the same direction as $\widehat{n}$, it follows that

$$wN^2(\pi b^2 dz) = -g'u_e(2\pi b dz) + g'w(z+dz)(\pi b) - g'w(z)(\pi b^2).$$

(A.20)

where g' is the reduced gravity. Rearranging (A.20) gives the buoyancy flux,

$$\frac{d(wg'\pi b^2)}{dz} = \pi w b^2 N^2.$$

(A.21)

Equations (A.9), (A.14) and (A.21) can be represented in terms of the volume flux, $Q = \pi w b^2$, momentum flux, $M = \pi w^2 b^2$ and buoyancy flux, $F = \pi g' w b^2$ respectively by

$$\frac{dQ}{dz} = 2\alpha \pi^{1/2} \sqrt{M},$$

(A.22)

$$\frac{dM}{dz} = \frac{FQ}{M} \tag{A.23}$$

and

$$\frac{dF}{dz} = QN^2. \tag{A.24}$$

The volume, momentum and buoyancy fluxes that determine the characteristics of a turbulent forced plume are defined respectively by

$$Q = 2\pi \int_0^\infty \bar{w} r dr = \pi \bar{w} b^2, \tag{A.25}$$

$$M = 2\pi \int_0^\infty \bar{w}^2 r dr = \pi \bar{w}^2 b^2 \tag{A.26}$$

and

$$F = 2\pi \int_0^\infty \bar{w} g' r dr = \pi \bar{w} g' b^2. \tag{A.27}$$

A.6 Gaussian Profile

The velocity and density profiles across the horizontal level of the plume is Gaussian in shape and given respectively by

$$w(r, z) = w_g(z) e^{-\left(\frac{r}{b}\right)^2}, \tag{A.28}$$

and

$$g'(r, z) = g'_g(z) e^{-\left(\frac{r}{\lambda b}\right)^2} \tag{A.29}$$

where b is the radius in the velocity and density profiles and λ is a constant of the order 1 (assuming that plume spreads symmetrically) where λb forms the characteristic radius in the density profile.

Substituting (A.28) and (A.29) into (A.22)-(A.24) we obtain

$$\frac{d(\pi b^2 w_g)}{dz} = 2\alpha\pi w, \tag{A.30}$$

$$\frac{d(\frac{1}{2}\pi b^2 w_g^2)}{dz} = \pi g_g' \lambda^2 b^2 \tag{A.31}$$

and

$$\frac{d\left(\pi b^2 w_g g_g'\left(\frac{\lambda^2}{1+\lambda^2}\right)\right)}{dz} = \pi b^2 w_g N^2 \tag{A.32}$$

which relate the fluxes to the Gaussian velocity and density profiles of the plume.

Appendix B

Scaling Analysis: spreading rate of radial intrusion in uniform stratification

A turbulent plume of density, ρ_0, is created from the injection of a source fluid with constant volume flux, Q_0, into a uniformly stratified ambient fluid of density, ρ_{00}. The plume fluid will rise to a maximum height then collapses axisymmetric to its neutral buoyancy level spreading radially outwards as an intrusive gravity current of thickness, $h(t)$, in time, t.

Assuming no entrainment across the thin interface between the radial spreading intrusion and surrounding ambient. The conservation of volume continuity equation becomes (Huppert, 1982)

$$Q_0 t \sim h(t) R_{\text{f}}^2, \tag{B.1}$$

where R_{f} is the radial distance travelled by the intrusion front and the intrusion thickness, h is constant in position but varies in time (Ungarish, 2009). From the pressure distribution over the volume of the intrusion, the radial

pressure gradient force acting on the limits that bound the intrusion in a box (Didden and Maxworthy, 1982; Huppert, 1982)

$$\frac{\partial p}{\partial r} = \Delta \rho g \frac{\partial h}{\partial r}, \tag{B.2}$$

where p is the pressure, g is the gravitational acceleration, $\Delta \rho$ is the density difference between the ambient and source fluids and $r \equiv R_{\mathrm{f}}$. From this it follows that the buoyancy force associated with the intrusion radial spread at its neutral buoyancy level is given by the product of the pressure and cross sectional area,

$$F_B \sim \Delta \rho g h^2 R_{\mathrm{f}}. \tag{B.3}$$

The horizontal momentum conservation equation for an intrusion spread in the buoyancy-inertia regime is given by

$$\frac{\partial p}{\partial r} = \rho_{00} u \frac{\partial u}{\partial r}. \tag{B.4}$$

where the intrusion front speed, $u_{\mathrm{f}} = R_{\mathrm{f}}/t$. Assuming that the intrusion first forms at the plume centreline, the inertial force associated with the spreading intrusion is

$$F_I \sim \frac{\rho_{00} h R_{\mathrm{f}}^3}{t^2}. \tag{B.5}$$

Balancing Equations (B.3) and (B.5) and using (B.1), we found that

$$R_{\mathrm{f}} \sim (g'Q_0)^{1/4} t^{3/4}, \tag{B.6}$$

gives the power law relationship for the radial spreading intrusion in the buoyancy-inertia regime.

It follows from (2.18) that the Froude number is (Sutherland et al., 2007;

93

Barenblatt, 1978)

$$\text{Fr} = \frac{u}{Nh}, \tag{B.7}$$

where N is the buoyancy frequency, u is the front speed and h is the intrusion thickness.

The law of volume conservation states that the supplied volume flow rate to a radial intrusion emanating from the centreline of a plume is

$$Q = 2\pi Ruh. \tag{B.8}$$

From the combination of (B.7) and (B.8) (Devenish and Rooney, 2014) showed that the intrusion front speed is given by

$$u = \frac{dR}{dt} = \left(\frac{\text{Fr}NQ}{2\pi}\right) R^{-1/2}, \tag{B.9}$$

when spreading in the buoyancy-inertia regime where the stratification, volume flux and Froude number are constant. Assuming that the initial radial position of the intrusion is first formed at the plume centreline it follows from (B.9) that the intrusion spreads radially as

$$R = \left(\frac{3}{2}\right)^{2/3} \left(\frac{\text{Fr}NQ}{2\pi}\right)^{1/3} t^{2/3}, \tag{B.10}$$

that predicts the spread as a different power-law in the buoyancy-inertia regime for $R \gg R_1$. From (B.10) the intrusion speed, u, can also be given by

$$u = \left(\frac{3}{2}\right)^{-1/3} \left(\frac{\text{Fr}NQ}{2\pi}\right)^{1/3} t^{-1/3}. \tag{B.11}$$

The reduce gravity, g' of a well mixed intrusion spreading in a stably stratified

ambient is (Ungarish, 2006)

$$g' = \frac{Nh}{2}. \tag{B.12}$$

Combine (B.7) and (B.12) rewrites g' as

$$g' = \frac{Nu}{2\mathrm{Fr}}, \tag{B.13}$$

Assume a constant supply of buoyancy flux to the radial spreading intrusion Equations (B.11) and (B.13) produce

$$R = \left(\frac{3}{2}\right)^{3/4} \left(\frac{\mathrm{Fr}^2 g' Q}{\pi}\right)^{1/4} t^{3/4}, \tag{B.14}$$

which also shows the power-law relationship of the radial spreading intrusion in the buoyancy-inertia regime. Equations (B.6) and (B.14) use two different assumptions, but predict intrusion spread in time as $R_\mathrm{f} \sim t^{3/4}$.

Bibliography

Abraham, G. (1967), Jet with negative buoyancy in homogeneous fluids, J. Hydr. Res., 5, 235–248.

Adcroft, A., R. Hallberg, J. Dunne, B. L. Sammuels, J. Galt, C. Barker, and D. Payton (2010), Simulations of underwater plumes of dissolved oil in the Gulf of Mexico, Res. Lett., 37, L18,605–L24,808.

Ansong, J. K., and B. R. Sutherland (2010), Internal gravity waves generated by convective plumes, J. Fluid Mech., 648, 405–434.

Baines, P. G., and R. S. J. Sparks (2005), Dynamics of giant volcanic ash clouds from supervolcanic eruptions, Geophys. Rev. Lett., 32, L24,808, doi:10.1029/2005GL024597.

Baines, W. D. (1983), Direct measurement of volume flux of a plume, J. Fluid Mech., 132, 247–256.

Barenblatt, G. I. (1978), Dynamics of turbulent spots and intrusions in stably stratified fluid, Sci. Atmos. Oceanic Phys., 14, 139–145.

Bloomfield, L. J., and R. C. Kerr (1998), Turbulent fountains in a stratified fluid, J. Fluid Mech., 358, 335–356.

Bloomfield, L. J., and R. C. Kerr (1999), Turbulent fountains in a confined stratified environment, J. Fluid Mech., 389, 27–54.

Bloomfield, L. J., and R. C. Kerr (2000), A theoretical model of a turbulent fountain, J. Fluid Mech., 424, 197–216.

Bolster, D., A. Hang, and P. F. Linden (2008), The front speed of intrusions into a continuously stratified medium, J. Fluid Mech., 594, 369–377.

Briggs, G. (1969), Plume rise, Tech. Rep. TID-25075, NTIS, USAEC Critical Review Series.

Brooks, N. H. (1972), Dispersion in hydrologic and coastal environments, Ph.D. thesis, California Institute of Technology, Pasadena, California.

Brooks, N. H., and R. C. Y. Koh (1965), Discharge of sewage effluent from a line source into a stratified ocean, 11th International Congress of International Association for Hydraulic Research, Leningrad, Russia.

Burridge, H. C., and G. R. Hunt (2012), The rise heights of low- and high-Froude number turbulent axisymetric fountains, J. Fluid Mech., 691, 392–416.

Camilli, R., C. M. Reddy, D. R. Yoeger, B. A. S. V. Mooy, M. Jakuba, J. Kinsey, C. McIntyre, S. Syla, and J. Maloney (2010), Tracking hydrocarbon plume transport and biodegradation at deepwater horizon, Science, 330, 201–204.

Carey, S. N., H. Sigurdsson, and R. S. J. Sparks (1986), Experimental studies of particle-laden plumes, J. Geo. Res., 93(B12), 15,314–15,328.

Caulfield, C. P., and A. W. Woods (1992), A laboratory study of explosive volcanic eruptions, Geophys. & Astrophys. Fluid Dyn., 97, 6699–6712.

Caulfield, C. P., and A. W. Woods (1995), Plumes with non-monotonic mixing behaviour, J. Geophys. Res., 79, 173–199.

Chen, J. (1980), Studies on gravitationally spreading currents, Ph.D. thesis, Califoria Institute of Technology.

Costa, A., A. Folch, and G. Macedonio (2006), A three-dimensional Eulerian model for transport and deposition of volcanic ashes, Earth Planet Sci. Lett., 241, 634–647.

Costa, A., A. Folch, and G. Macedonio (2010), A model for wet aggregation of ash particles in volcanic plumes and clouds: 1. theoretical formulation, J. Geophys. Res., 115, B09,201, doi:10.1029/2009JB007175.

Costa, A., A. Folch, and G. Macedonio (2013), Density-driven transport in the umbrella region of volcanic clouds: Implications for tephra dispersion models., Earth Planet Sci. Lett., 40, 4823–4827.

Crapper, P. F., and W. D. Baines (1976), Non-Boussinesq forced plumes, Atmos. Env., 11, 415–420.

Devenish, B. J., and G. Rooney (2014), Plume rise and spread in a linearly stratified environment, Geophys. & Astrophys. Fluid Dyn., pp. 1–23, doi:10.1080/03091929.2013.849345.

Devenish, B. J., G. Rooney, and D. J. Thomson (2010), Large-eddy simulation of a buoyant plume in uniform and stably stratified environments, J. Fluid. Mech., 652, 75–103.

Didden, N., and T. Maxworthy (1982), The viscous spreading of plane and axisymmetric gravity currents, J. Fluid Mech., 121, 27–42.

Fan, L. (1967), Turbulent buoyant jets into stratified or flowing ambients, Ph.D. thesis, California Institute of Technology, Pasadena, California.

Fox, D. G. (1970), Forced plume in stratified fluid, J. Geophys. Res., 75(33), 6818–6835.

Frias-Torres, S. Bostater, and J. R. Charles (2011), Potential impacts of the Deepwater Horizon oil spill on large pelagic fishes, in Remote sensing of the Ocean, sea ice, coastal waters and large water regions 2011, vol. 8175, edited by C. R. Bostater, S. Mertikas, and X. Neyt, pp. 81,750F–81,750F–7, SPIE, Proceedings of SPIE, Prague, Central Europe.

Gerbhart, B. L., A. W. Schorr, and A. W. Pera (1970), Steady laminar natural convection plumes above a horizontal line heat source, Int. J. Heat Mass Transfer, 13, 116–171.

Helfrich, K. R., and T. M. Batisti (1991), Experiments on baroclinic vortex shedding from hydrothermal plumes, J. Geophy. Res., 96(C7), 12,511–12,518.

Heskestad, G. (2014), Dynamics of the fire plume, Phil. Trans. R. Soc. Lond., 356, 2815–2833.

Holasek, R. E., A. W. Woods, and S. Self (1995), Wind-driven dispersal of volcanic ash plumes and its control on the thermal structure of the plume-top, Bull. Volcanol., 57, 283–292.

Holasek, R. E., A. W. Woods, and S. Self (1996a), Experiments on gas - ash separation processes in volcanic umbrella plumes, J. Volcanol. Geotherm. Res., 70, 169–181.

Holasek, R. E., S. Self, and A. W. Woods (1996b), Satellite observations and interpretation of the 1991 Mount Pinatubo eruption plumes, J. Geophys. Res., 101, 27,635–27,655.

Huppert, H. E. (1982), The propagation of two-dimensional and axisymmetric viscous gravity currents over a rigid horizontal surface, J. Fluid Mech., 121, 43–58.

Huppert, H. E., and J. E. Simpson (1980), The slumping of gravity currents, J. Fluid Mech., 99, 785–799.

Ivey, G. N., and S. Blake (1985), Axisymmetric withdrawal and inflow in a density-stratified container, J. Fluid Mech., 161, 115–137.

Joseph, H. L., and H. C. Vincent (2003), Turbulent jets and plumes-A Lagrangian approach, Kluwer Academic, Massachusetts, USA.

Kaminski, T., and G. Carazzo (2005), Turbulent entrainment in jets with arbitrary buoyancy, J. Fluid Mech., 526, 361–376.

Kaye, N. (2008), Turbulent plumes in stratified environments: A review of recent work, Atmos. Oceans, 46, 433–441.

Kotsovinos, N. (2000), Axisymmetric submerged intrusion in stratified fluid, J. Hydraulic Engineering, ASCE, 126, 446–456.

Koyaguchi, T. (1994), Grain-size variation of tephra derived from volcanic umbrella clouds, Bull. Volcanol., 56, 1–9.

Koyaguchi, T., and M. Tokuno (1993), Origin of the giant eruption cloud of Pinatubo, June 15, 1991, J. Volcanol. Geotherm. Res., 55, 85–96.

Lee, J., and V. Chu (2003), Turbulent buoyant jets and plumes: A Langrangian approach, Kluwer Academic Publishers, Dordrecht, The Netherlands.

Lemckert, C., and J. Imberger (1993), Axisymmetric intrusive gravity currents in linearly stratified fluids, J. Hydraulic Engineering, ASCE, 119, 662–679.

List, E. J. (1979), Mixing in Inland and Coastal Waters-Turbulent jets and plumes, 315–389 pp., Academic Press Inc., San Deigo.

List, E. J. (1982), Turbulent jets and plumes, Annu. Rev. Fluid Mech., 14, 189–212.

Lister, J. R., and R. C. Kerr (1989), The propagation of two-dimensional and axisymmetric viscous gravity currents at a fluid interface, J. Fluid Mech., 203, 215–249.

Maxworthy, T. (1972), Experimental and theoretical studies of horizontal jets in a stratified fluid, in Proc. Int. Symp. on Stratified Flows, pp. 611–618, Int. Assoc. for Hydraulic Res. Delft, Netherlands, Russia, Novosibirsk.

McDougall, T. J. (1978), Bubble plumes in stratified environments, J. Fluid Mech., 85, 655–672.

McDougall, T. J. (1981), Negatively buoyant vertical jets, Tellus, 33, 313–320.

Mollendorf, J. C., and B. Gerbhart (1973), Thermal buoyancy in round laminar vertical jets, Int. J. Heat Mass Transfer, 16, 735–745.

Morton, B. R. (1959), Forced plumes, J. Fluid Mech., 5, 151–163.

Morton, B. R. (1962), Coaxial turbulent jets, Intl J. Heat Mass Transfer, 5, 955–965.

Morton, B. R., G. I. Taylor, and J. S. Turner (1956), Turbulent gravitational convection from maintained and instantaneous sources, Proc. R. Soc. London, Ser. A, 234, 1–23.

Oster, G. (1965), Density gradients, Sci. Am., 213, 70.

Priestley, C. H. B., and F. K. Ball (1955), Continous convection from an isolated source of heat, Quartley Journal of Royal Meteorological Society, 81(384), 144–156.

Richards, T. S., Q. Aubourg, and B. R. Sutherland (2014), Radial intrusions from turbulent plumes in uniform stratification, Phys. Fluids, 26, 036,602–1–036,602–17.

Robi, W. (1982), Turbulent buoyant jets and plumes, 192 pp., Pergamon Press.

Robock, A. (2004), Climatic impact of volcanic emission, Geophys. Mono. Ser., 19, 125–134.

Scase, M. M., C. P. Caulfield, and S. B. Dalziel (2006), Boussinesq plumes and jets with decreasing source strengths in stratified environments, J. Fluid Mech., 564, 305–331.

Shabbir, A., and W. K. George (1994), Experiments on a round turbulent buoyant plume, J. Fluid Mech., 275, 1–32.

Sparks, R., S. Carey, J. Gilbert, L. Glaze, H. Sigurdsson, and A. W. Woods (1997), Volcanic Plumes, John Wiley, Chichester, U. K.

Sparks, R. S. J., J. G. Moore, and C. J. Rice (1986), The initial giant umbrella cloud of the May 18, 1980 eruption of Mount St-Helens, J. Volcanol. Geothermal Res., 28, 257–274.

Sutherland, B. R., A. N. F. Chow, and T. P. Pittman (2007), The collapse of a mixed patch in stratified fluid, Phys. Fluids, 19, 116,602–1–6, doi:10.1063/1.2814331.

Textor, C., H. F. Graf, M. Herzog, J. M. Oberhuber, W. I. Rose, and G. Ernst (2006), Volcanic particle aggregation in explosive eruption column. Part I: Parameterization of the microphysics of hydrometeors and ash, J. Volcanology Geothermal Research, 150, 359–377.

Turner, J. S. (1966), Jets and plumes with negative or reversing buoyancy, J. Fluid Mech., 26, 779–792.

Ungarish, M. (2006), On gravity currents in a linearly stratified ambient: A generalization of Benjamin's steady-state propagation results, J. Fluid Mech., 548, 49–68.

Ungarish, M. (2009), An Introduction to Gravity Currents and Intrusions, 489 pp., Chapman and Hall/CRC press, New York.

Ungarish, M., and T. Zemach (2012), The flow of high-Reynolds axisymmetric gravity currents of a stratified fluid into a startified ambient: shallow-water and box model solutions, J. Fluid Mech., 12, 347–359.

Williams, D. B., and H. E. Thomas (2011), An assessment of volcanic hazards to aviation-a case study from the 2009 Sarychev peak eruption, Geo. Nat. Haz. and Risk, 2(3), 233–246, doi:10.1080/19475705.2011.558117.

Wilson, L., R. S. J. Sparks, T. C. Huang, and N. D. Watkins (1978), The control of volcanic column heights by eruption energetics and dynamics, J. Geophys. Res., 83(B4), 1829–1836.

Woods, A. W. (1988), The fluid dynamics and thermodynamics of eruption columns, Bul. Volcano., 50, I69 –193.

Woods, A. W. (2010), Turbulent plumes in nature, Ann. Rev. Fluid Mech., 42, 391–412.

Yapa, P. D., and F. Chen (2004), Behaviour of oil and gas from deepwater blowouts, J. Hyd. Eng., 6, 540–553.

Yapa, P. D., and L. Zheng (1997), Modelling oil and gas releases from deep water: A review, Tech. Bull., 4, 189–198.

Zarrebini, M., and S. S. Cardoso (2000), Patterns of sedimentation from surface currents generated by turbulent plumes, J. AIChE, 46(10), 1947–1956.

Zatsepin, A., and G. Shapiro (1982), A study of axisymmetric intrusions in a stratified fluid, Izvestiya, Atmosph. and Ocean Phys., 18, 77–80.

Zielinski, G. A. (2002), Climatic impacts of volcanic eruptions, J. Scientific World, 2, 869–884.